

Supporting Information

Evaluating topologically diverse metal-organic frameworks for cryo-adsorbed hydrogen storage

Diego A. Gómez-Gualdrón^{a,‡}, Yamil J. Colón^{a,‡}, Xu Zhang^{b,‡}, Timothy C. Wang^c, Yu-Sheng Chen^d, Joseph T. Hupp^c, Taner Yildirim^{e,*}, Omar K. Farha^{c,f,*}, Jian Zhang^{b,*}, Randall Q. Snurr^{a,*}

^a Department of Chemical & Biological Engineering, Northwestern University, 2145 Sheridan Road, Evanston, IL 60208-3120 (USA)

^b Department of Chemistry, University of Nebraska-Lincoln, Lincoln, NE 68588-0304 (USA)

^c Department of Chemistry, Northwestern University, 2145 Sheridan Road, Evanston, IL 60208-3113 (USA)

^d ChemMatCARS, Center for Advanced Radiation Sources, The University of Chicago, 9700 S. Cass Avenue, Lemont, Illinois 60439 (USA)

^e NIST Center for Neutron Research, National Institute of Standards and Technology, Gaithersburg, MD 20899 (USA)

^f Department of Chemistry, Faculty of Science, King Abdulaziz University, Jeddah 22254 (Saudi Arabia)

[‡] These authors contributed equally to this work

*e-mail: snurr@northwestern.edu, jzhang3@unl.edu, o-farha@northwestern.edu, taner@nist.gov

TABLE OF CONTENTS

Section S1 Computational MOF construction	S3-S12
Section S2 Simulation methods	S13-S16
Section S3 Histograms and structure-property relationships	S17-S22
Section S4 Examples of constructed MOFs with deliverable capacity	S23-S25
Section S5 Experimental procedures and materials	S26-S26
Section S6 Ligand and MOF synthesis procedures	S27-S44
Section S7 Single crystal X-ray structures determination	S45-S47
Section S8 TGA data	S48-S49
Section S9 MOF activation and BET area determination	S50-S54
Section S10. Hydrogen adsorption measurements	S55-S56
Section S11 References	S57-S58

Section S1. Computational MOF construction

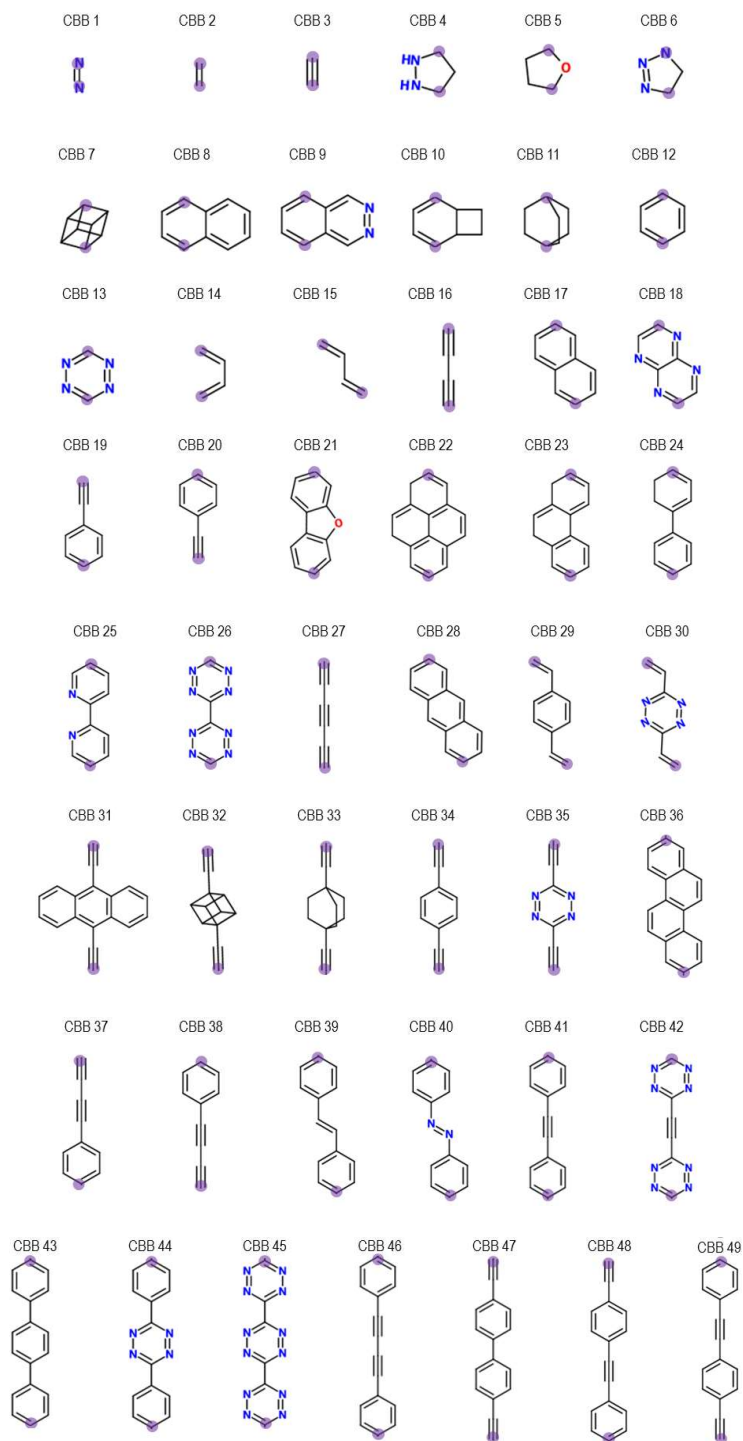


Figure S1. Connecting building blocks (CBBs) used to construct the 13,512 MOFs investigated in this work. Translucent purple points denote connecting atoms. Note that “CBB 0” represents the case when organic and inorganic nodes are connected directly (e.g. “CBB 0” is the connecting building blocks in the well-known MOF **HKUST-1**)

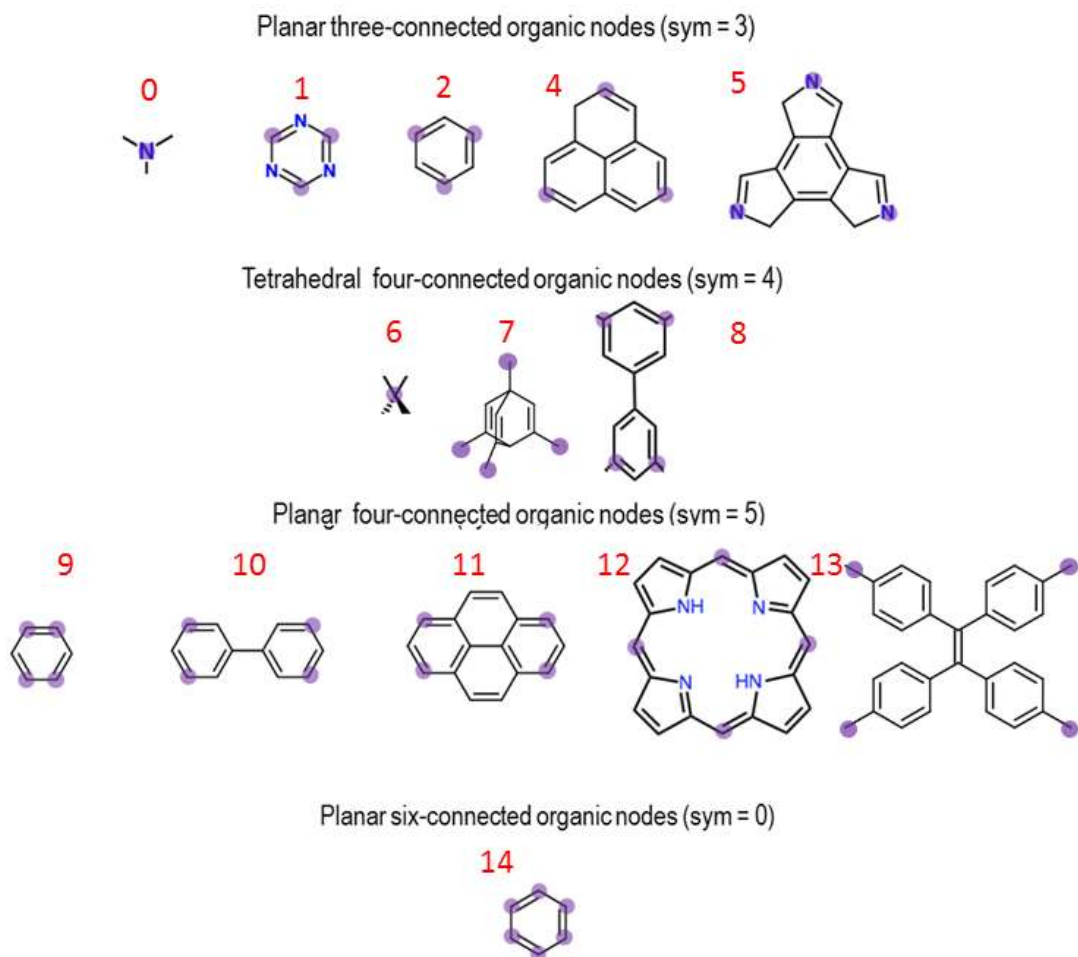


Figure S2. Organic nodular building blocks used to construct the 13,512 MOFs investigated in this work. Translucent purple points denote connecting atoms. The “sym” parameter that lets the code know what is the symmetry of the building block. For instance, sym = 3 indicates three-fold planar symmetry, sym = 4 indicates four-fold tetrahedral symmetry, sym = 5 indicates four-fold planar symmetry, and sym = 0 indicates six-fold planar symmetry. Red number indicates the ID of the building block during MOF construction.

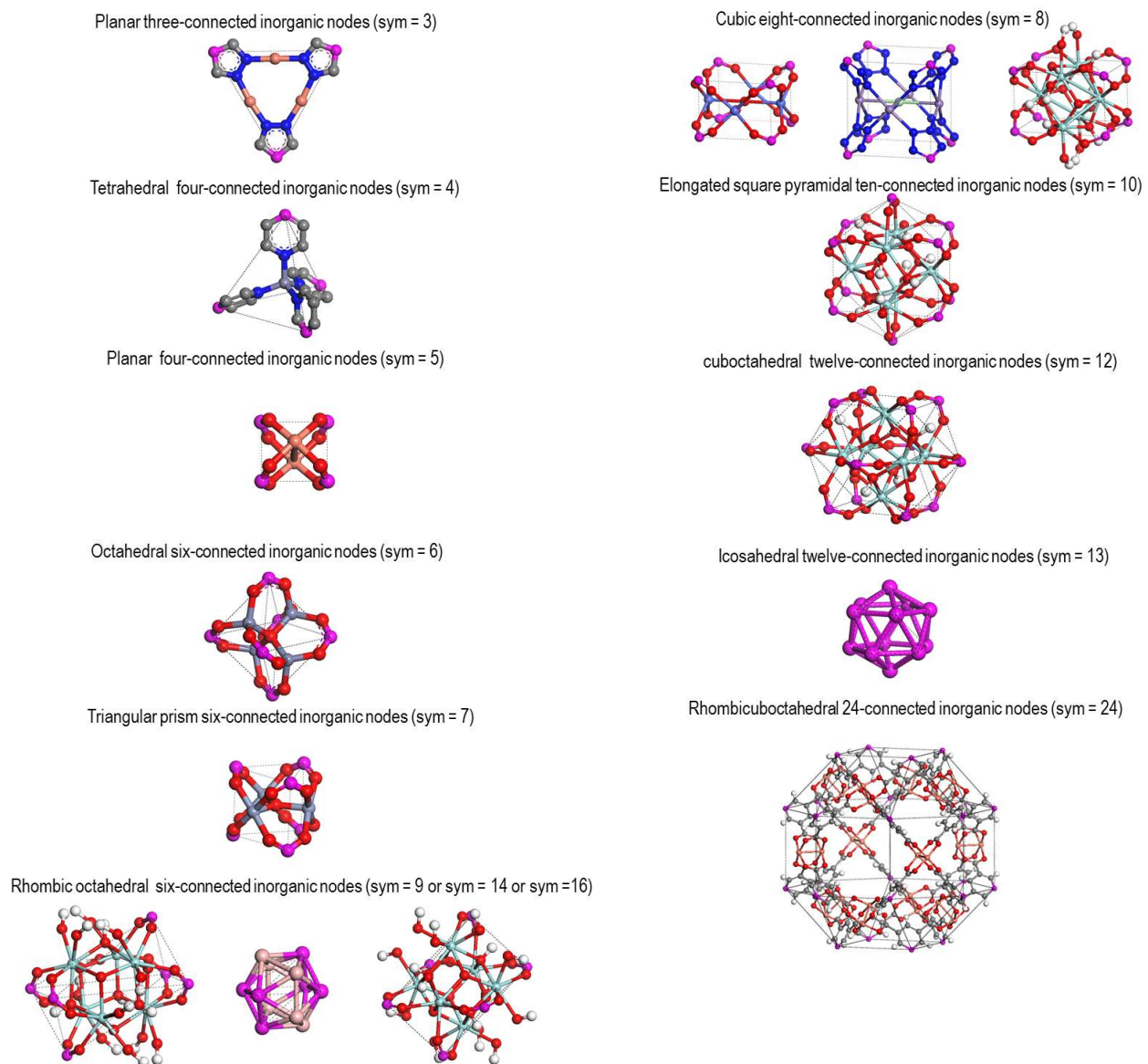


Figure S3. Inorganic nodular building blocks used to construct the 13,512 MOFs investigated in this work. Pink color denotes connecting atoms.

Table S1. Information for topological blueprints (nodes in red and green, edges in blue). ^a symmetry codes (sym) according to Figure S3. ^b Number of nodes and edges are given per unit cell.

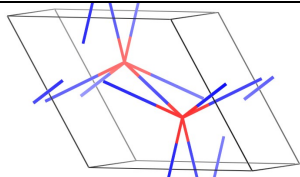
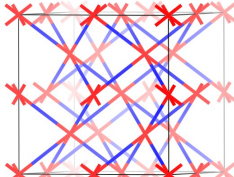
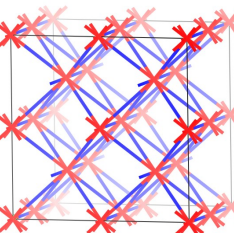
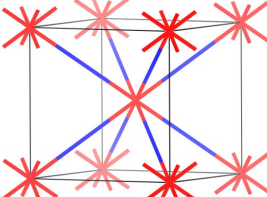
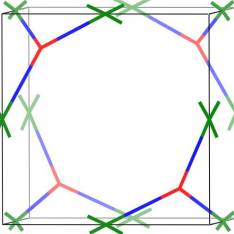
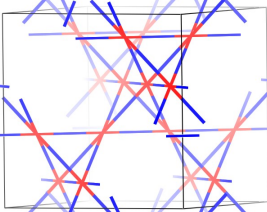
Topological Blueprint	Topology name	Nodes connectivity	Nodes “sym” code ^a	Number of nodes ^b	Number of edges ^b
	acs	6	7	2	6
	bcs	6	16	16	48
	bct	10	10	16	80
	bcu	8	8	2	8
	bor	3-4	3-4	4-3	12
	crs	6	9	16	48

Table S1. Continuation.

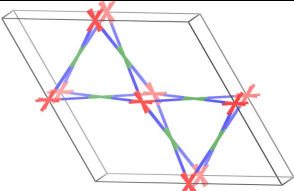
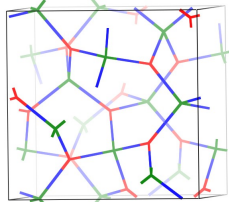
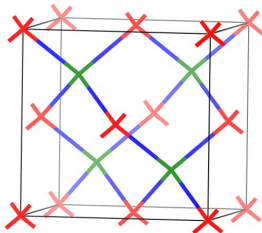
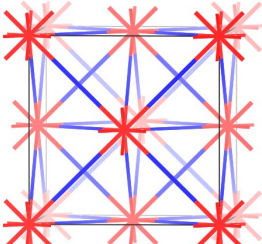
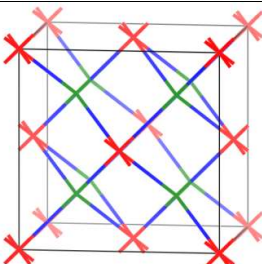
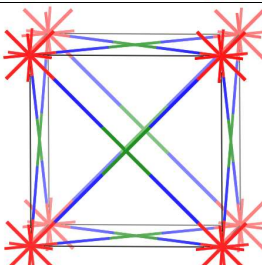
Topological Blueprint	Topology name	Nodes connectivity	Nodes “sym” code^a	Number of nodes^b	Number of edges^b
	csq	4-8	5-8	6-3	24
	ctn	3-4	3-4	16-12	48
	dia	4-4	4-4	4-4	16
	fcu	12	12	4	24
	flu	4-8	4-8	8-4	32
	ftw	4-12	5-12	3-1	12

Table S1. Continuation.

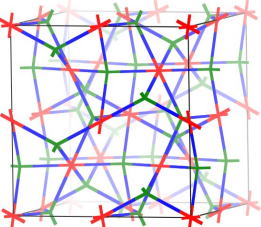
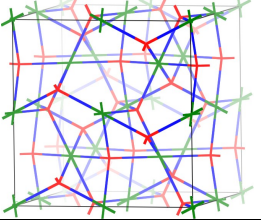
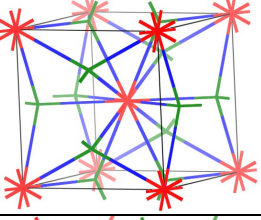
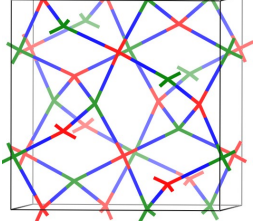
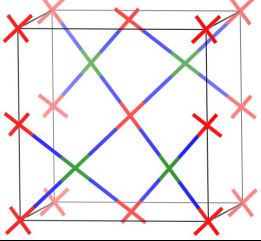
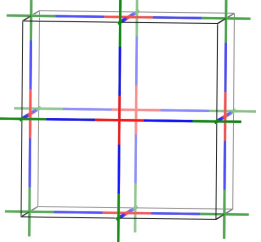
Topological Blueprint	Topology name	Nodes connectivity	Nodes “sym” code^a	Number of nodes^b	Number of edges^b
	gar	4-6	4-16	24-16	96
	iac	4-6	4-9	24-16	96
	ith	4-12	4-13	6-2	24
	lcs	4-4	4-4	12-12	48
	lvt	4-4	5-5	4-4	16
	nbo	4-4	5-5	3-3	12

Table S1. Continuation.

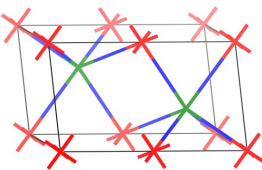
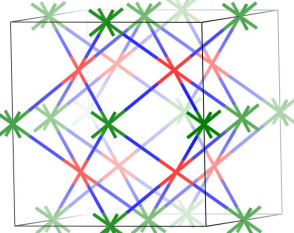
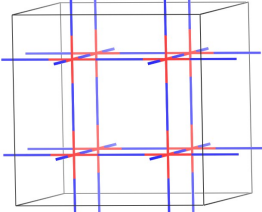
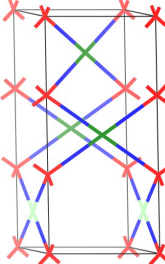
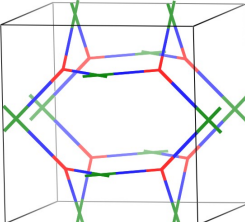
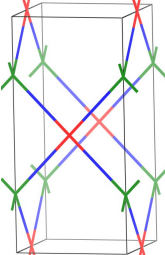
Topological Blueprint	Topology name	Nodes connectivity	Nodes “sym” code^a	Number of nodes^b	Number of edges^b
	nia	6-6	6-7	2-2	12
	ocu	6-8	16-8	8-6	48
	pcu	6	6	8	24
	pth	4-4	4-5	3-3	12
	pto	3-4	3-5	8-6	24
	pts	4-4	5-4	2-2	8

Table S1. Continuation.

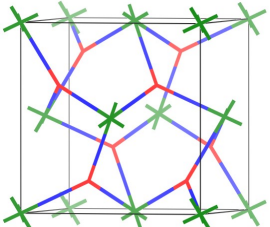
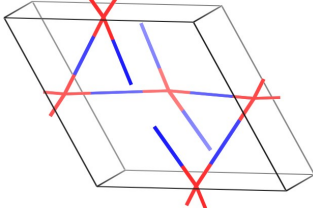
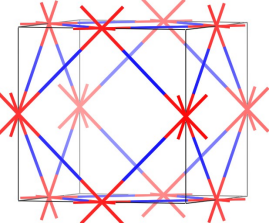
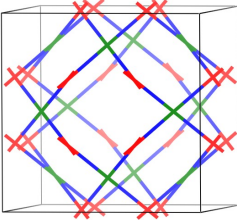
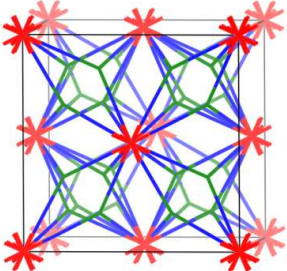
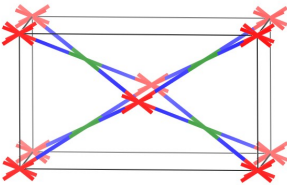
Topological Blueprint	Topology name	Nodes connectivity	Nodes “sym” code^a	Number of nodes^b	Number of edges^b
	pyr	3-6	3-6	8-4	24
	qtz	4	4	3	6
	reo	8	8	3	12
	rhr	4-4	5-5	12-12	48
	rht	3-24	3-24	32-4	96
	scu	4-8	5-8	4-2	16

Table S1. Continuation.

Topological Blueprint	Topology name	Nodes connectivity	Nodes “sym” code^a	Number of nodes^b	Number of edges^b
	she	4-6	5-0	12-8	48
	soc	4-6	5-9	12-8	48
	sod	4-4	4-4	6-6	24
	spn	3-6	3-9	32-16	96
	srs	3-3	3-3	4-4	12
	ssa	4-4	5-5	6-6	24

Table S1. Continuation.

Topological Blueprint	Topology name	Nodes connectivity	Nodes “sym” code^a	Number of nodes^b	Number of edges^b
	ssb	4-4	5-5	8-8	32
	stp	4-6	5-7	3-2	12
	tbo	3-4	3-5	32-24	96
	the	3-8	3-8	8-3	24
	tpt	4-6	5-7	3-2	12

Section S2. Simulation methods

Structural optimization. Optimization of the automatically constructed MOF structures was done using the same strategy we have used in previous work, where we had applied it to much smaller numbers of structures.^{1,2} Namely, each MOF structure was optimized in two steps. First, each structure undergoes a constrained optimization with the unit cell shape and dimensions remaining constant. Then, each optimized structure undergoes a full (unconstrained) optimization. Optimizations were done using the Forcite module of Materials Studio.³ The optimization convergence criteria were 2×10^{-5} kcal/mol, 1×10^{-3} kcal/mol/Å and 1×10^{-5} Å for energies, forces, and displacements, respectively. During optimizations, no electrostatic interactions were considered and both bonded and non-bonded interactions between MOF atoms were described using the generic Universal Force Field⁴ with a 12.0 Å cutoff for non-bonded interactions. With the Universal Force Field, non-bonded interactions are described according to the Lennard-Jones potential

$$V_{ij} = 4\varepsilon_{ij} \left[\left(\frac{\sigma_{ij}}{r_{ij}} \right)^{12} - \left(\frac{\sigma_{ij}}{r_{ij}} \right)^6 \right]$$

where i and j are interacting atoms, r_{ij} is the their interatomic distance, ε_{ij} is their LJ potential well depth, σ_{ij} is the distance at which repulsion between i and j occurs. When i and j are different types of atoms, ε_{ij} and σ_{ij} were calculated using Lorentz-Berthelot mixing rules.

One distinct advantage of our automated MOF construction procedure is that it creates crystallographic information files (CIFs) having all the necessary connectivity information for Materials Studio to automatically assign the correct MOF atom types. Therefore, the 13,512 constructed MOFs were directly optimized by Materials Studio with the assistance of a simple script. The accuracy of optimized MOF structures using the Universal Force Field has been thoroughly discussed in previous work.¹ For illustration purposes, **Figure S4** overlaps some experimental MOF structures with the equivalent ones obtained with our automated MOF construction procedure. Nevertheless, note that the constructed structures can, if desired, be optimized with more specialized force fields such as UFF4MOF developed by Addicoat *et al.*⁵ and MOF-FF developed by Bureekaew *et al.*⁶

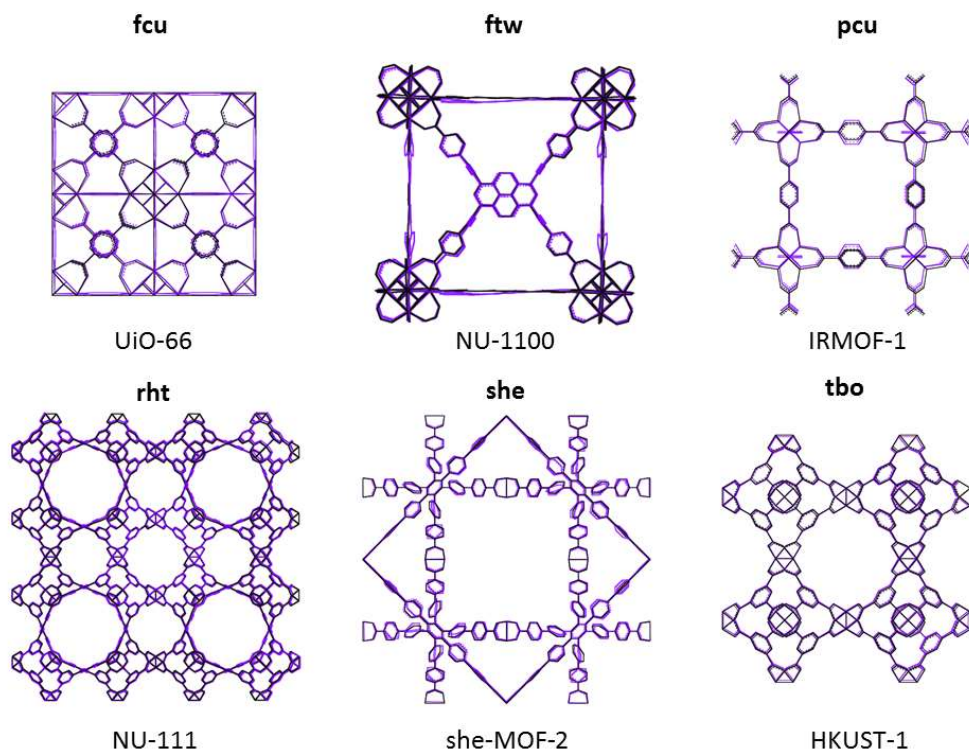


Figure S4. Overlap between a topologically diverse set of experimental MOF structures (black) and the equivalent structures obtained with our automated MOF construction procedure (purple). The topology and common name of the MOFs are found above and below each structure. Experimental structures were obtained from ref. ⁷ for **UiO-66**, ref. ⁸ for **NU-1100**, ref. ⁹ for **IRMOF-1**, ref. ¹⁰ for **NU-111**, ref. ¹¹ for **HKUST-1**, and from single-crystal X-ray diffraction (*vide infra*) for **she-MOF-2**.

Hydrogen adsorption. Grand canonical Monte Carlo (GCMC) simulations were performed using our simulation code RASPA.¹² Hydrogen uptakes for hydrogen pressures of 5 bar/160 K and 100 bar/77 K were simulated for all 13,512 MOFs. Each simulation consisted of 1,000 equilibration cycles followed by 2,000 cycles to calculate ensemble averages. Complete adsorption isotherms at 77 K up to 150 bar hydrogen pressures were performed for **she-MOF-1**, **she-MOF-2**, **she-MOF-3**, and **she-MOF-4**. Each simulation consisted of 5,000 equilibration cycles followed by 5,000 cycles to calculate ensemble averages. Each cycle consists of N moves where N corresponds to the maximum between 20 and the number of molecules in the system. Equal-probability moves for hydrogen molecules consisted of insertions, deletions, translations, rotations, and reinsertions. MOF atoms remained fixed at their crystallographic positions during simulations. $l \times m \times n$ MOF supercells were used with l , m , and n as needed to satisfy the minimum image convention.

Hydrogen fugacity was calculated from the gas-phase temperature and pressure using the Peng-Robinson equation of state. Non-bonded MOF-hydrogen and hydrogen-hydrogen interactions were modeled using a Lennard Jones (LJ) potential with Feynman Hibbs (FH) corrections¹³ and Coulomb interactions:

$$V_{ij} = \frac{4\varepsilon_{ij} \hbar^2}{r_{ij}^2 24 \mu_{ij} k_B T} \left[132 \left(\frac{\sigma_{ij}}{r_{ij}} \right)^{12} - 30 \left(\frac{\sigma_{ij}}{r_{ij}} \right)^6 \right] + \frac{q_i q_j}{4\pi \epsilon_0 r_{ij}}$$

where \hbar and k_B are the reduced Planck constant and the Boltzmann constant, respectively, i and j are interacting atoms, r_{ij} is their interatomic distance, q_i and q_j are their partial charges, ε_{ij} is their LJ potential well depth, σ_{ij} is the distance at which repulsion between i and j occurs, μ_{ij} is the reduced mass of interacting atoms i and j , and ϵ_0 is the dielectric constant. When i and j are different types of atoms, ε_{ij} and σ_{ij} were calculated using Lorentz-Berthelot mixing rules.

No charges were placed on the MOF atoms, whose LJ parameters were taken from the Universal Force Field (UFF).⁴ (**Table S2**) Hydrogen molecules were modeled as rigid, using a single LJ sphere at the center of mass which was taken from the Michels-Degraaff-Tenseldam model.¹⁴ Charges were placed at the nuclei (+0.468) and the center of mass (-0.936) according to the Darkrim-Levesque model¹⁵ (**Table S3**). A cutoff of 12.8 Å was used for all LJ interactions and Ewald summations were used for Coulomb interactions.

Table S2. LJ parameters for framework atoms.

Atom type	ε/k_B (K)	σ (Å)
H	22.14	2.57
B	135.86	2.43
C	52.83	3.43
N	34.75	3.27
O	30.19	3.12
Si	156.00	3.80
Cr	7.55	2.69
Mn	6.54	2.64
Co	7.04	2.56
Cu	2.52	3.11
Zn	62.40	2.46
Zr	34.72	2.78
Cl	114.23	3.52

Table S3. LJ parameters and charges for hydrogen.

Adsorbate	ε/k_B (K)	σ (Å)	q
H	-	-	+0.468
H ₂ _COM	36.7	2.958	-0.936

Nitrogen adsorption. Complete adsorption isotherms at 77 K up to 1 bar nitrogen pressure were performed for **she-MOF-1**, **she-MOF-2**, **she-MOF-3**, and **she-MOF-4**. Each simulation consisted of 20,000 equilibration cycles followed by 20,000 cycles to calculate ensemble averages. Nitrogen fugacity was calculated using the Peng Robinson equation of state. Nitrogen molecules were modeled as rigid using a three-site model according to the TraPPE force field.¹⁶

Table S4. LJ parameters and charges for nitrogen

Adsorbate	ϵ/k_B (K)	σ (Å)	q
N	36.0	3.31	-0.462
N ₂ _COM	0.0	0.00	+0.964

MOF computational characterization. Surface areas of MOF structures were calculated by rolling a nitrogen probe over the framework atoms.¹⁷ Helium void fractions for the structures were calculated using Widom insertions.¹⁸ Heats of adsorption were calculated directly from GCMC simulations by applying the fluctuation theory.¹⁹ Pore limiting diameter (PLD) and largest cavity diameter (LCD) were calculated using the code Zeo++.²⁰ Calculations with Zeo++ used the high accuracy flag and considered framework atoms to be the same diameters as the σ parameters listed in Table S2.

Section S3. Histograms and structure-property relationships

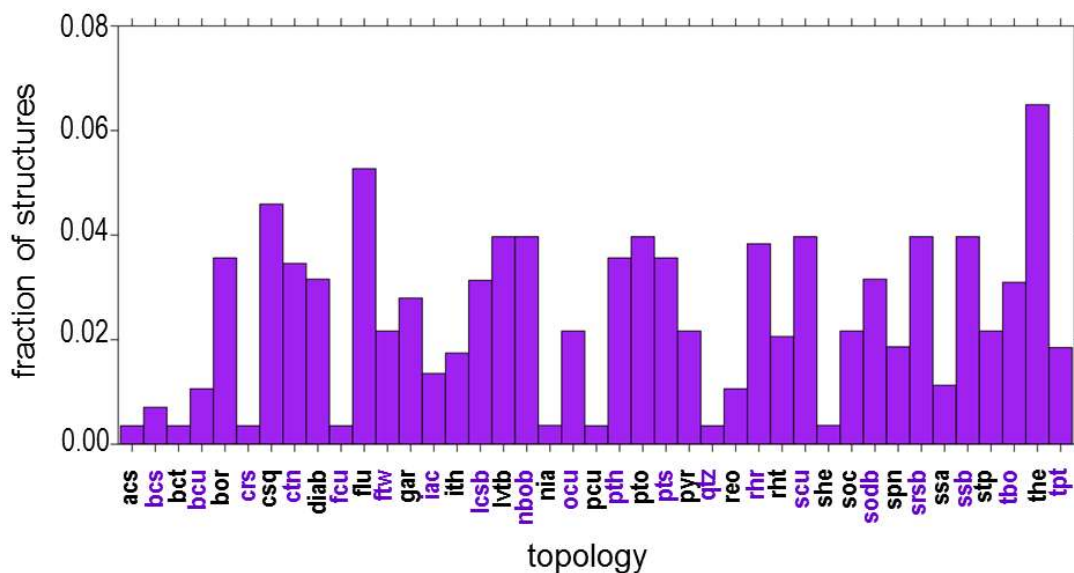


Figure S5. Histogram based on the topology of the 13,512 constructed MOFs.

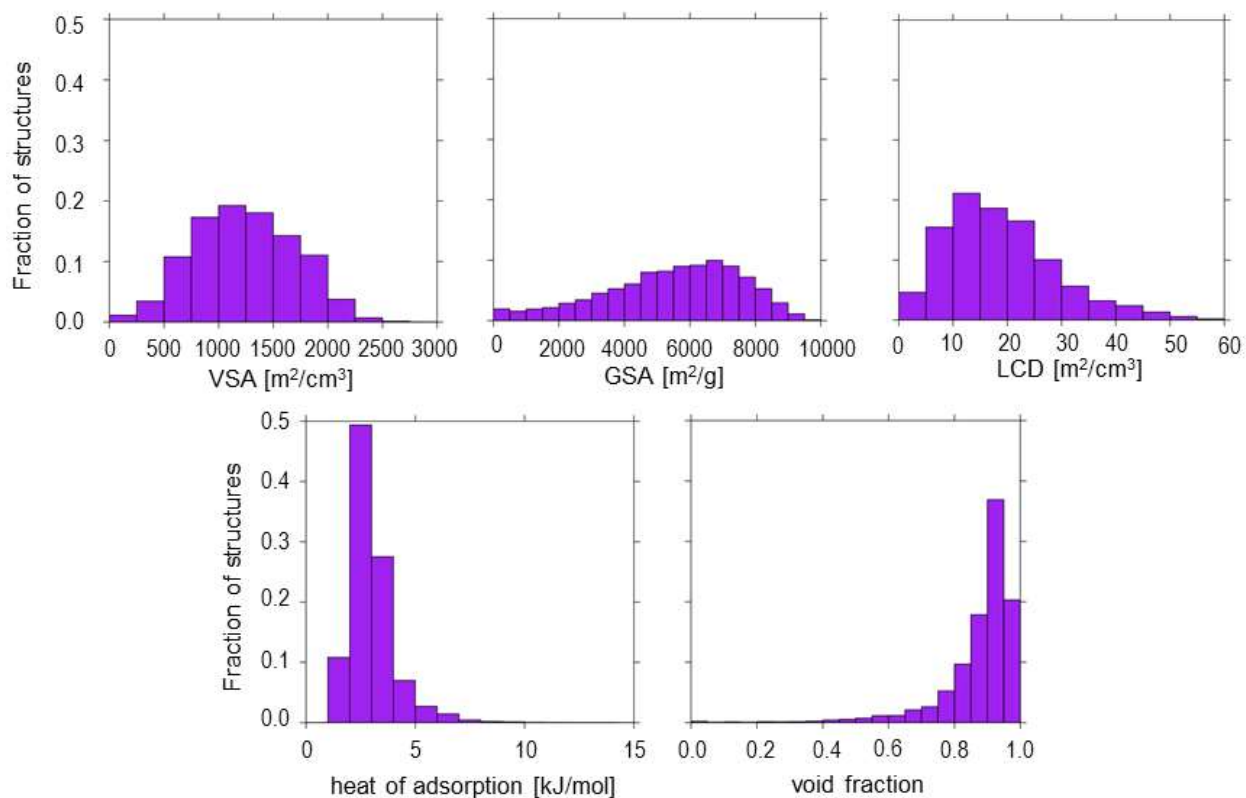


Figure S6. Histogram based on calculated textural and chemical properties of the 13,512 constructed MOFs. (VSA: volumetric surface area; GSA: gravimetric surface area; LCD: largest cavity diameter)

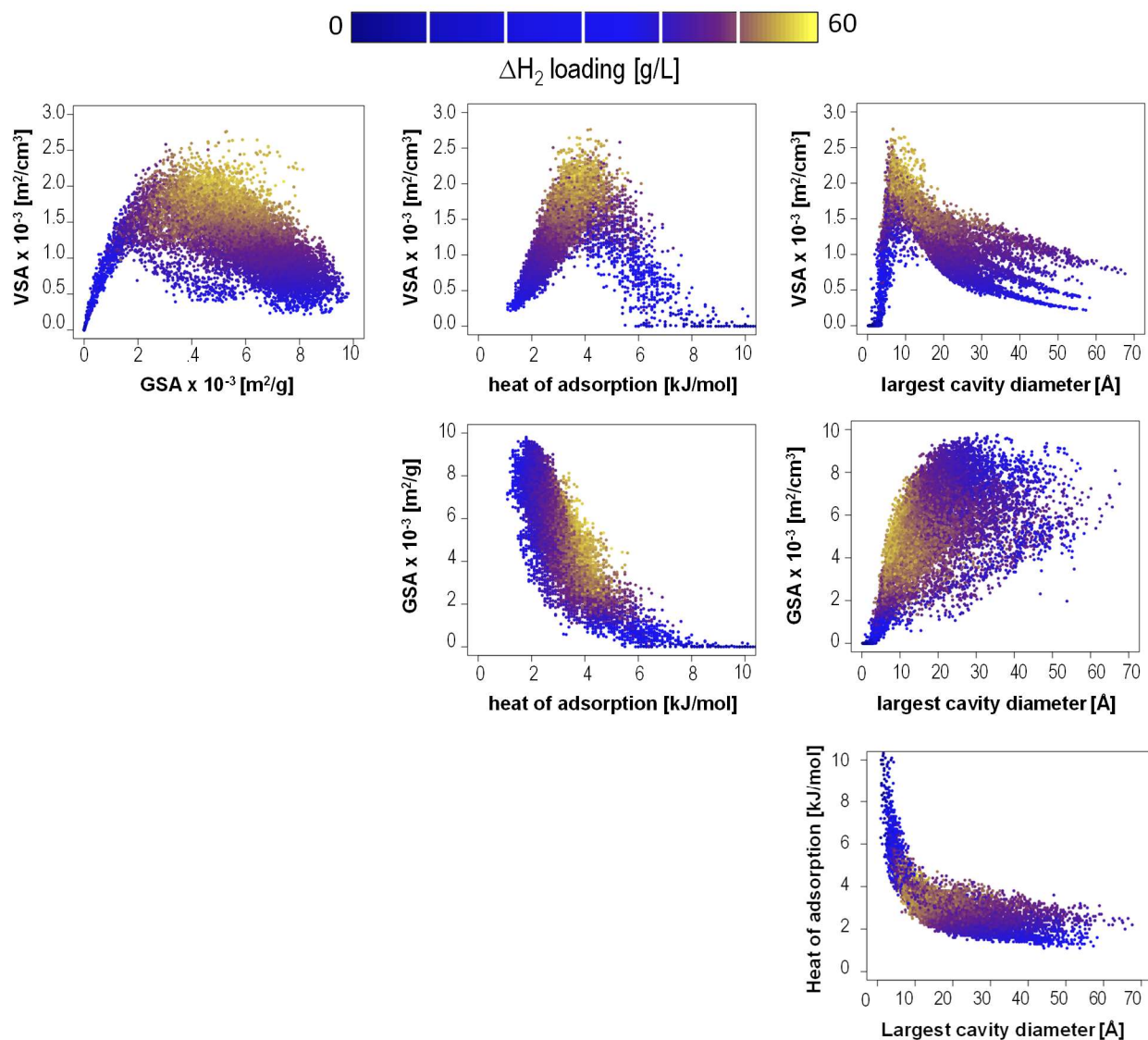


Figure S7. Relationships between calculated MOF properties with points colored according to the *volumetric* hydrogen deliverable capacity of the corresponding MOF according to the color scale bar at the top. (VSA: volumetric surface area; GSA: gravimetric surface area.) Note that any given point has the same color in all plots.

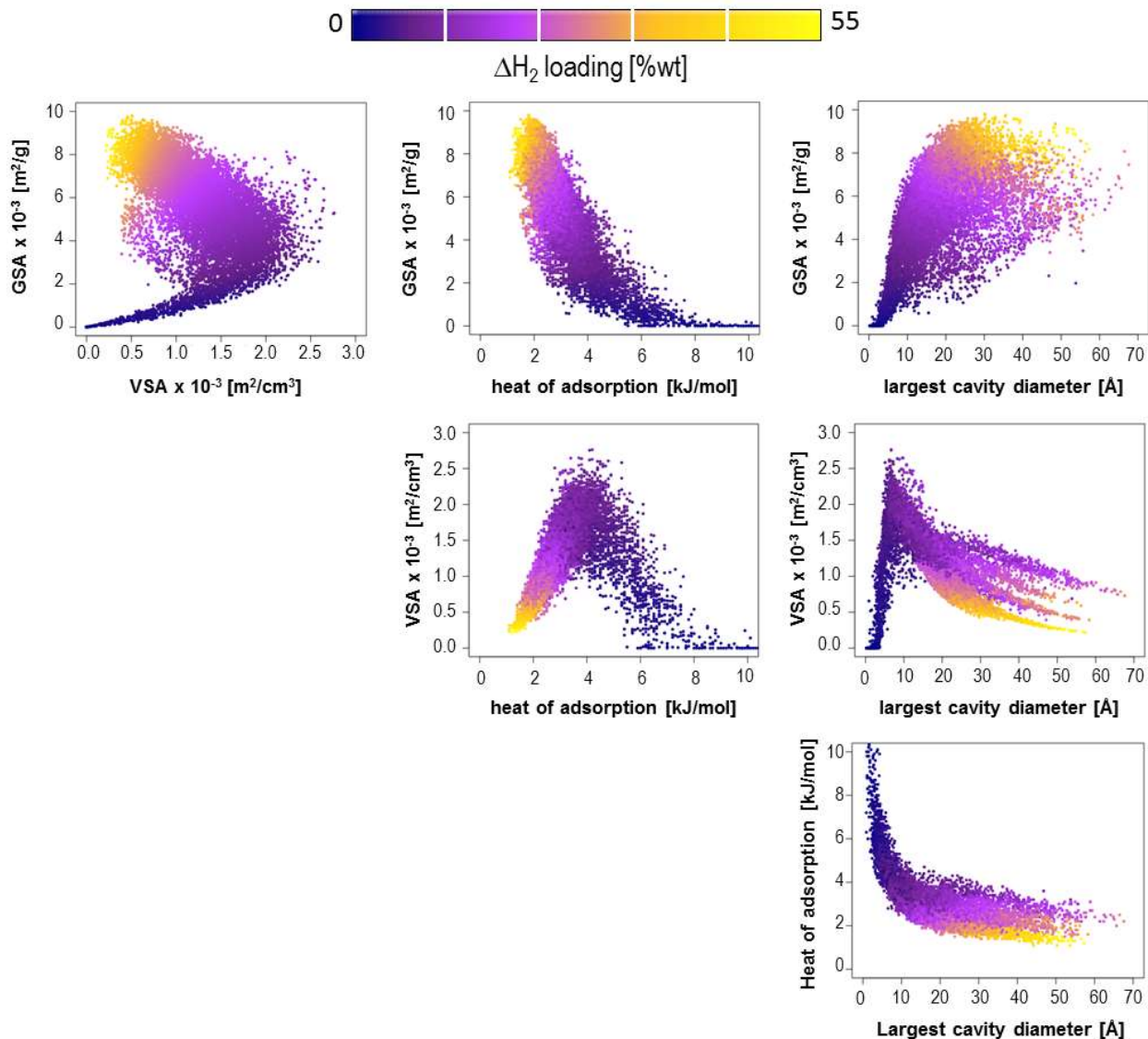


Figure S8. Relationships between calculated MOF properties with points colored according to the *gravimetric* hydrogen deliverable capacity of the corresponding MOF according to the color scale bar at the top. (VSA: volumetric surface area; GSA: gravimetric surface area.) Note that any given point has the same color in all plots.

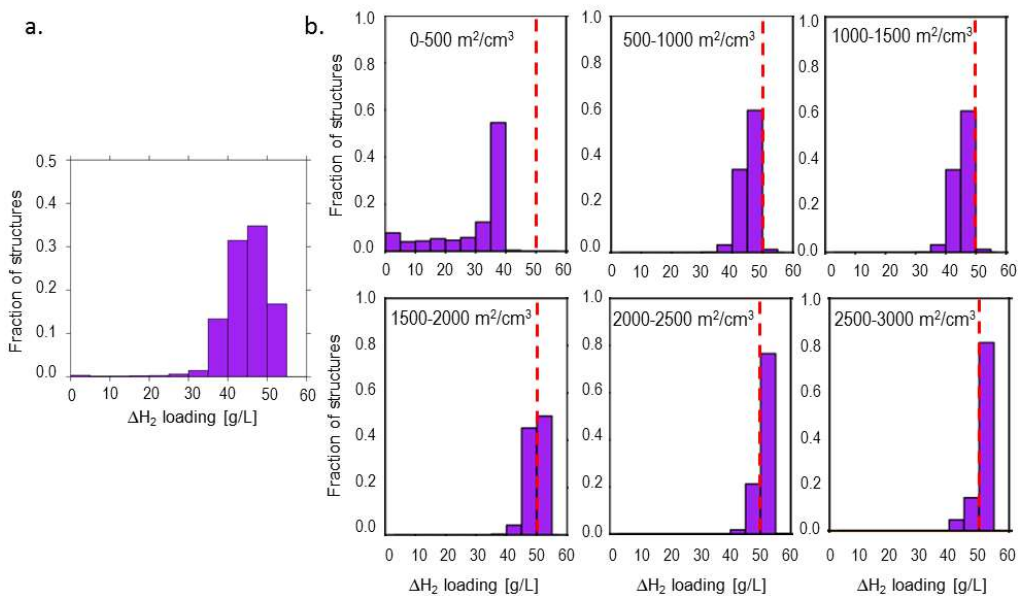


Figure S9. a) Histogram of volumetric hydrogen deliverable capacity for the 13,512 constructed MOFs. b) Histograms of volumetric hydrogen deliverable capacity for different subsets of MOFs based on the volumetric surface area (e.g. ca. 80% of MOFs with volumetric surface areas between 2,500 and 3,000 m^2/cm^3 have volumetric hydrogen deliverable capacities higher than 50 g/L). The red vertical line is placed as a reference for a volumetric deliverable capacity threshold of 50 g/L.

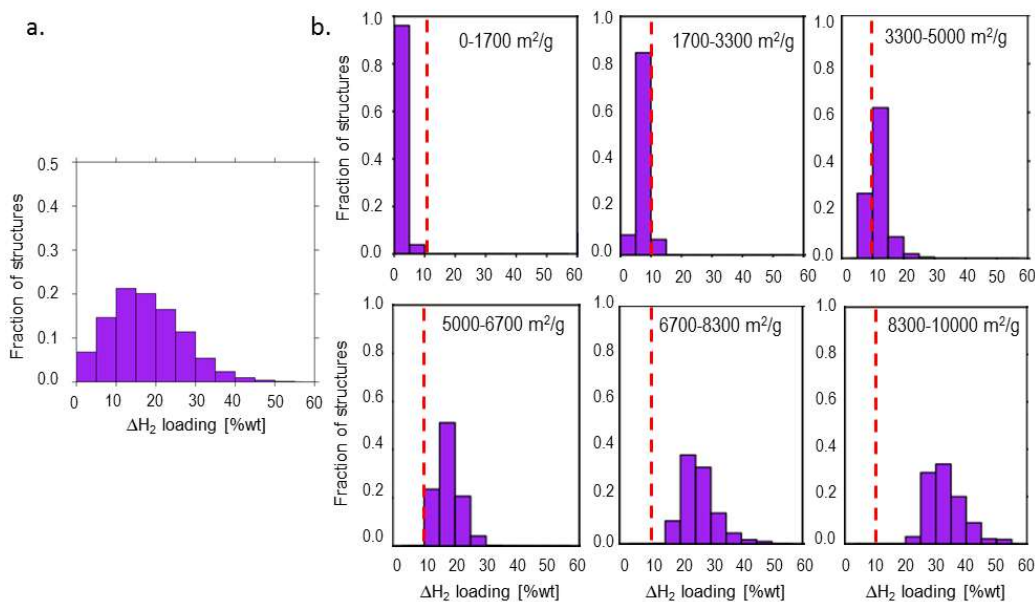


Figure S10. a) Histogram of gravimetric hydrogen deliverable capacity for the 13,512 constructed MOFs. b) Histograms of gravimetric hydrogen deliverable capacity for different subsets of MOFs based on the gravimetric surface area (e.g. ca. 100% of MOFs with gravimetric surface areas higher than 5,000 m^2/g have gravimetric hydrogen deliverable capacities higher than 10 wt%). The red vertical line is placed as a reference for a gravimetric deliverable capacity threshold of 10 wt%.

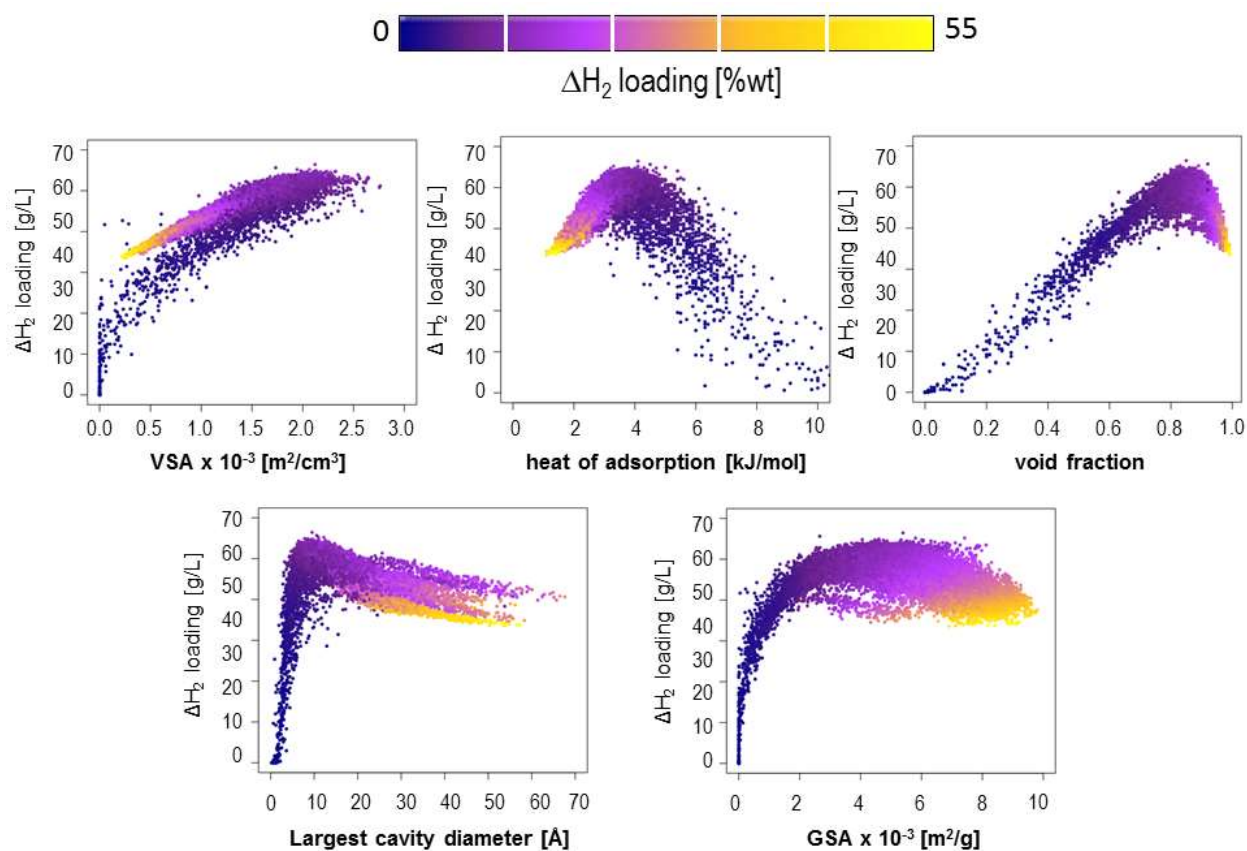


Figure S11. Relationships between volumetric hydrogen deliverable capacity and calculated textural and chemical properties for 13,512 MOFs with points colored according to the gravimetric hydrogen deliverable capacity based on the color bar at the top (identical to that of Figure S8). Note that any given point has the same color in all plots.

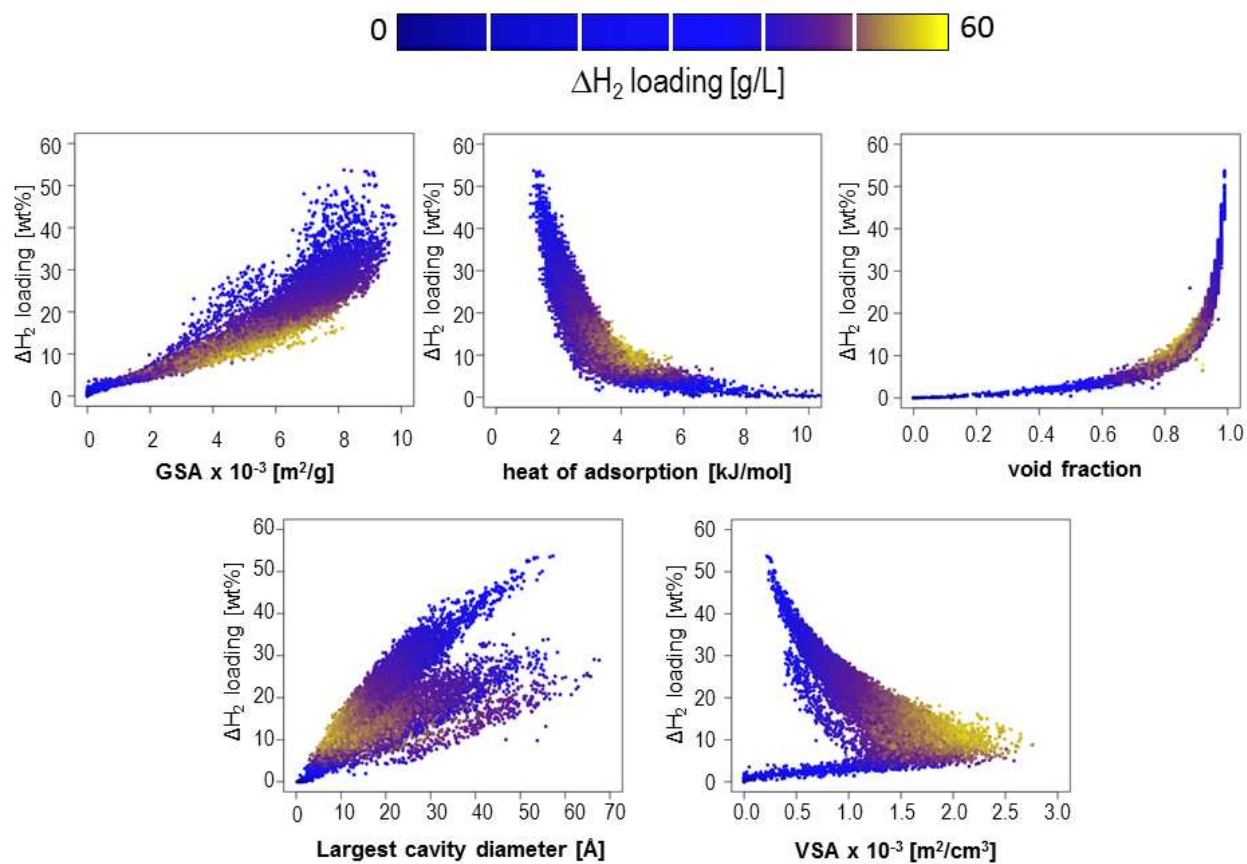


Figure S12. Relationships between gravimetric hydrogen deliverable capacity and calculated textural and chemical properties for 13,512 MOFs with points colored according to the volumetric hydrogen deliverable capacity based on the color bar at the top (identical to that of Figure S7). Note that any given point has the same color in all plots.

Section S4 Examples of constructed MOFs with high deliverable capacity

As noted in the main text, the highest volumetric deliverable capacity predicted for the 13,512 MOFs at the “100 bar/77 K → 5 bar/160 K” operating conditions is 57 g/L. For a number of MOFs, deliverable capacities higher than 50 g/L are predicted. We list some of these MOFs in Table S5 below along with some characterization information.

Table S5. Examples of constructed MOFs with high volumetric deliverable capacity. LCD = largest cavity diameter, PLD = pore limiting diameter.

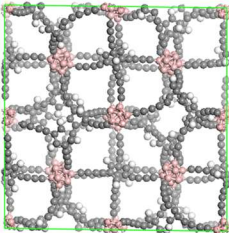
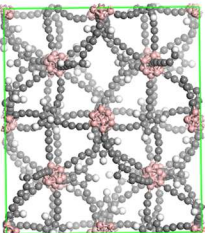
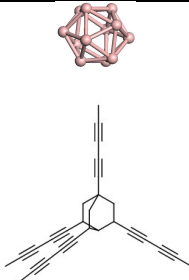
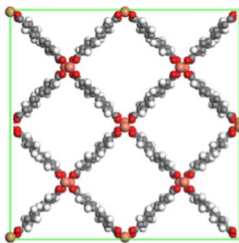
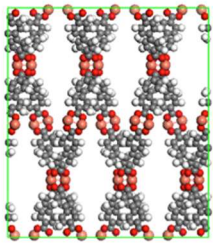
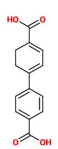
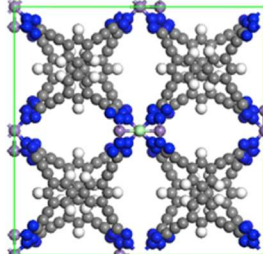
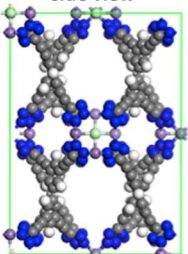
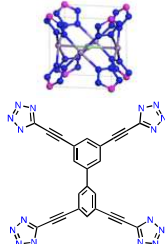
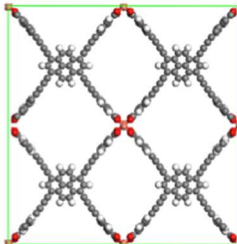
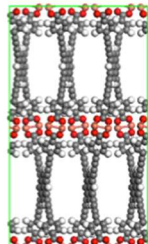
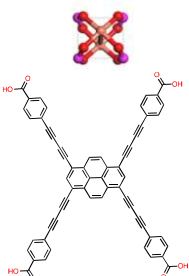
MOF Structure	Node and Linker	Information
<p>front view</p>  <p>side view</p> 	<p>Node and Linker</p> 	<p>Topology: gar Void fraction: 0.85 Vol. surface area: 2120 m²/cm³ LCD: 11.0 Å PLD: 9.5 Å Deliverable capacity: 56.9 g/L (6.0 %wt)</p>
<p>front view</p>  <p>side view</p> 	<p>Node and Linker</p>  	<p>Topology: lvt Void fraction: 0.88 Vol. surface area: 2317 m²/cm³ LCD: 12.9 Å PLD: 11.0 Å Deliverable capacity: 55.3 g/L (12.5 %wt)</p>
<p>front view</p>  <p>side view</p> 	<p>Node and Linker</p> 	<p>Topology: flu Void fraction: 0.84 Vol. surface area: 2098 LCD: 11.7 Å PLD: 6.4 Å Deliverable capacity: 54.8 g/L (10.1 %wt)</p>
<p>front view</p>  <p>side view</p> 	<p>Node and Linker</p> 	<p>Topology: lvt Void fraction: 0.87 Vol. surface area: 2064 m²/cm³ LCD: 13.5 Å PLD: 13.3 Å Deliverable capacity: 54.6 g/L (12.9 %wt)</p>

Table S2. Continuation

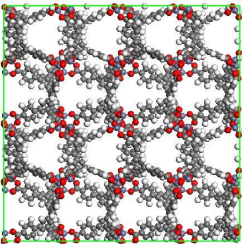
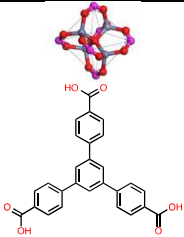
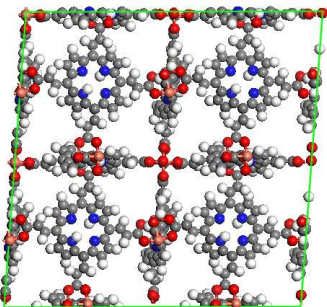
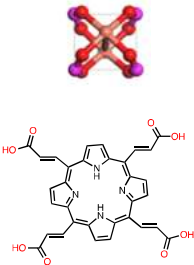
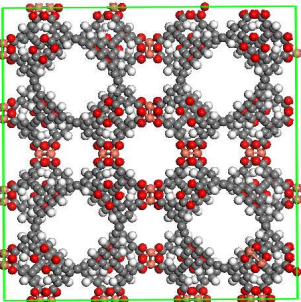
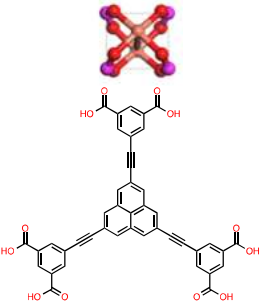
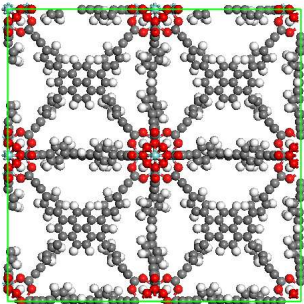
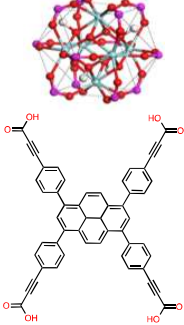
MOF	Node and Linker	Information
		<p>Topology: pyr Void fraction: 0.86 Vol. surface area: 2041 m²/cm³ LCD: 11.0 Å PLD: 9.2 Å Deliverable capacity: 55.2 g/L (11.0 %wt)</p>
		<p>Topology: nbo Void fraction: 0.84 Vol. surface area: 1954 m²/cm³ LCD: 14.6 Å PLD: 7.6 Å Deliverable capacity: 54.4 g/L (9.6 %wt)</p>
		<p>Topology: rht Void fraction: 0.86 Vol. surface area: 1924 m²/cm³ LCD: 20.9 Å PLD: 6.4 Å Deliverable capacity: 54.4 g/L (9.9 %wt)</p>
		<p>Topology: ftw Void fraction: 0.85 Vol. surface area: 2024 m²/cm³ LCD: 17.5 Å PLD: 7.4 Å Deliverable capacity: 54.2 g/L (10.0 %wt)</p>

Table S5. Continuation

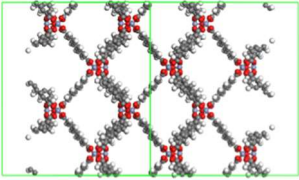
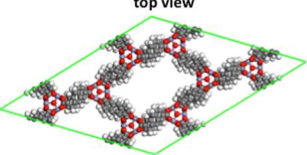
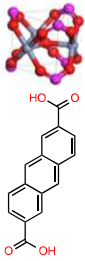
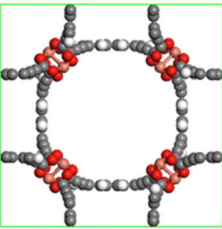
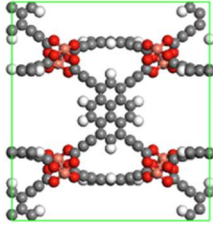
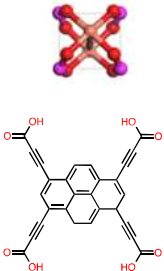
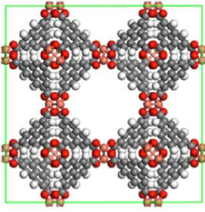
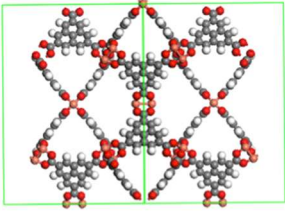
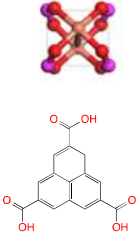
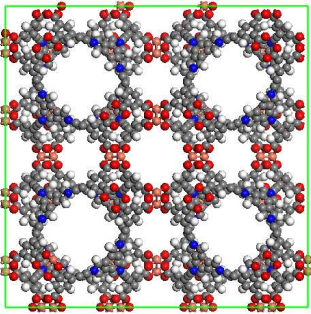
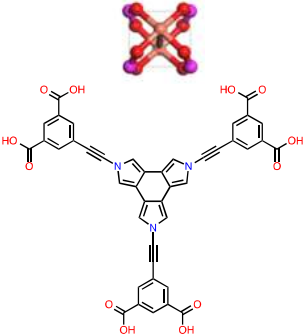
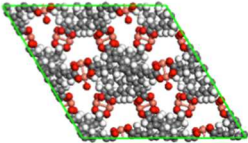
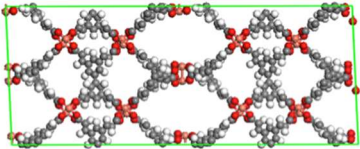
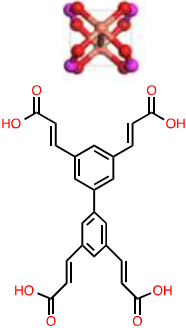
MOF	Node and Linker	Information
<p style="text-align: center;">Side-diagonal view</p>  <p style="text-align: center;">top view</p> 		<p>Topology: acs Void fraction: 0.86 Vol. surface area: 1971 m²/cm³ LCD: 12.6 Å PLD: 9.6 Å Deliverable capacity: 53.3 g/L (10.9 %wt)</p>
<p style="text-align: center;">front view</p>  <p style="text-align: center;">side view</p> 		<p>Topology: ssb Void fraction: Vol. surface area: 1904 m²/cm³ LCD: 17.0 Å PLD: 13.3 Å Deliverable capacity: 53.8 g/L (10.7 %wt)</p>
<p style="text-align: center;">front view</p>  <p style="text-align: center;">side-diagonal view</p> 		<p>Topology: tbo Void fraction: 0.85 Vol. surface area: 1885 m²/cm³ LCD: 17.5 Å PLD: 8.6 Å Deliverable capacity: 53.8 g/L (8.4 %wt)</p>
		<p>Topology: rht Void fraction: 0.86 Vol. surface area: 1916 m²/cm³ LCD: 21.1 Å PLD: 7.5 Å Deliverable capacity: 54.1 g/L (10.2 %wt)</p>

Table S5. Continuation

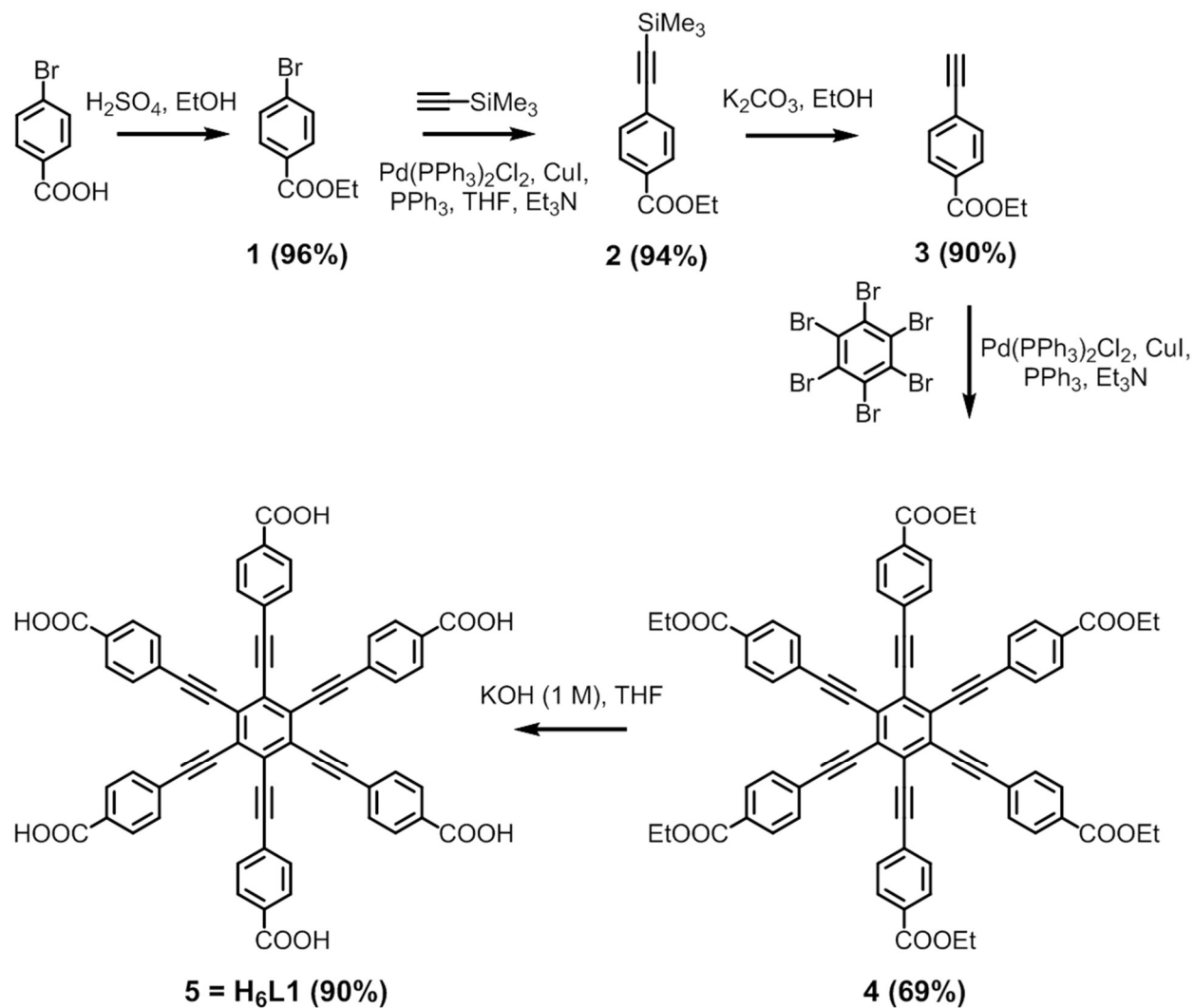
MOF	Node and Linker	Information
<p data-bbox="391 291 472 310">front view</p>  <p data-bbox="415 474 488 493">side view</p> 		<p data-bbox="1105 348 1268 380">Topology: pth</p> <p data-bbox="1105 380 1308 407">Void fraction: 0.84</p> <p data-bbox="1105 407 1349 434">Vol. surface area: 2191</p> <p data-bbox="1105 434 1235 462">LCD: 9.6 Å</p> <p data-bbox="1105 462 1235 489">PLD: 8.2 Å</p> <p data-bbox="1105 489 1333 558">Deliverable capacity: 52.7 g/L (9.58 %wt)</p>

Section S5. Experimental procedures and materials

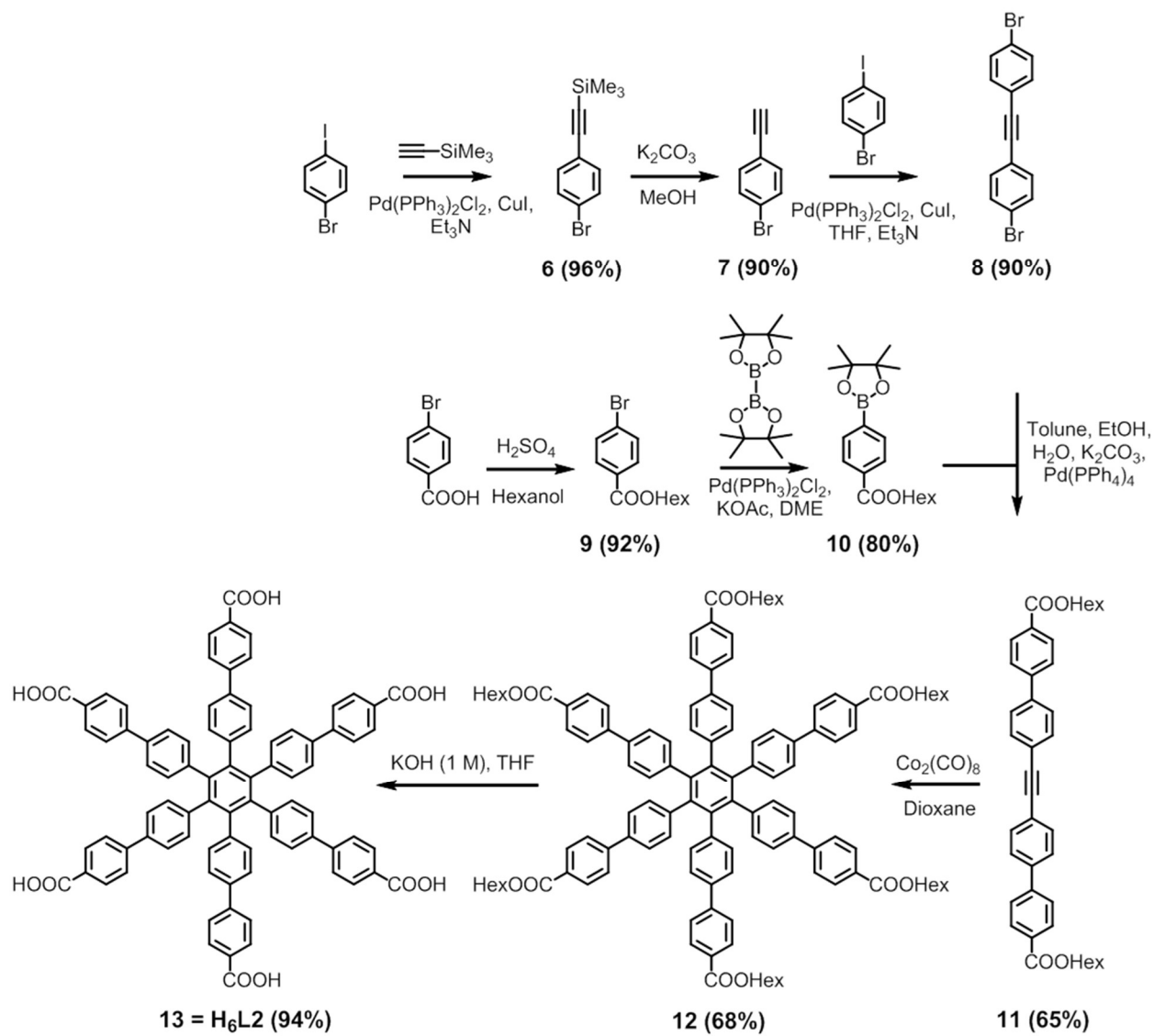
All solvents and reagents were purchased from commercial sources and, unless otherwise noted, used without further purification. All air-sensitive reactions were carried out using standard Schlenk techniques under argon. ^1H and ^{13}C NMR spectra were recorded on Bruker FT-NMR spectrometers (300 MHz or 400 MHz). Thermogravimetric analyses (TGA) were performed on a Netzsch STA 449C thermal analyzer from 30 to 700 °C under nitrogen atmosphere at a heating rate of 10 °C/minute rate. Infrared spectroscopy was performed on a Nicolet Avatar 360 FT-IR. PXRD data for **she-MOF-1**, **-2**, and **-3** were taken with a Bruker AXS DA X-ray diffractometer with a GADDS area detector, using the spinning capillary method. The copper target X-ray tube was set to 40 kV and 40 mA. PXRD data for **she-MOF-4** were recorded on a Rigaku Ultima IV diffractometer at 40 kV and 44 mA with a scan rate of 1.5 deg/min, using nickel-filtered Cu K α radiation ($\lambda = 1.5418$). MOF supercritical CO $_2$ activation was performed using a TousimisTM Samdri[®] PVT-3D critical point dryer (Tousimis, Rockville, MD, USA). N $_2$ adsorption measurements were performed at 77 K, with the temperature held constant using liquid N $_2$ bath. For **she-MOF-1**, the nitrogen isotherm of the activated sample was measured on an ASAP 2020 (Micromeritics, GA), and for **she-MOF-2** on a Tristar II (Micromeritics, GA).

Section S6. Ligand and MOF synthesis procedures

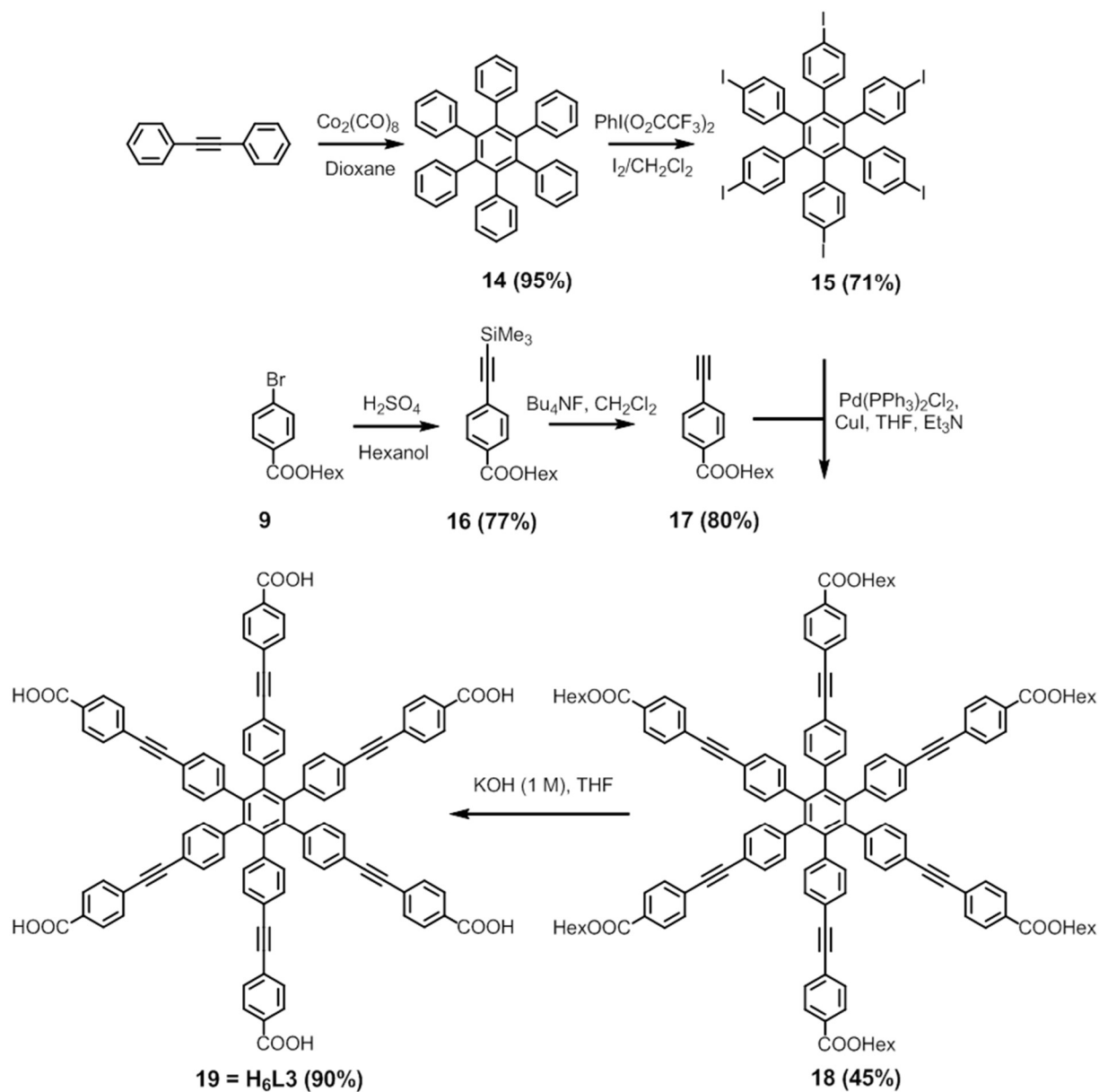
Synthesis of H₆L₁ and UNLSF-1:



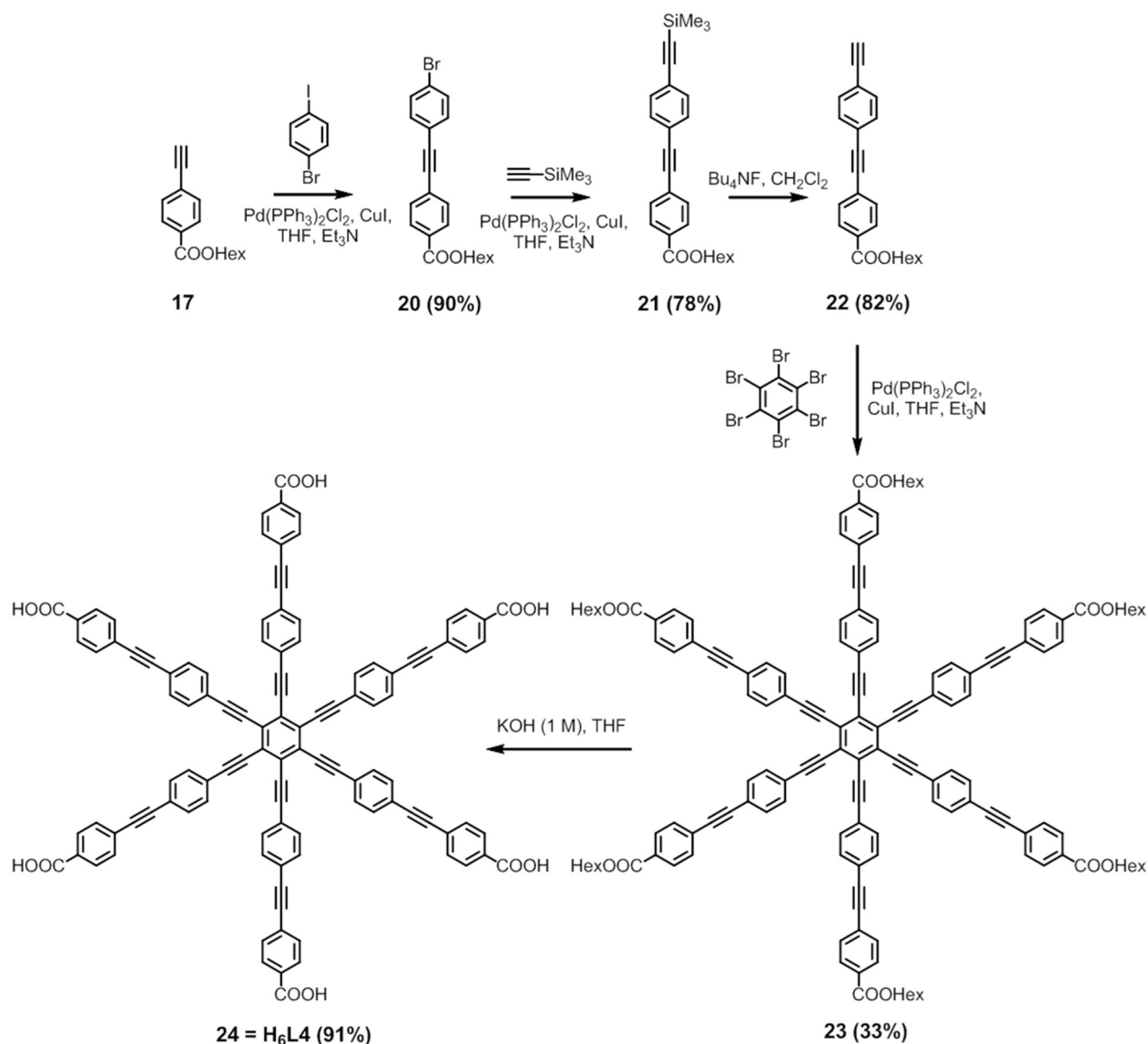
Scheme S1. Synthesis of ligand **5 (H₆L₁)**.



Scheme S2. Synthesis of ligand **13 (H₆L2)**.



Scheme S3. Synthesis of ligand **19 (H₆L3)**.



Scheme S4. Synthesis of ligand **24** (H₆L4).

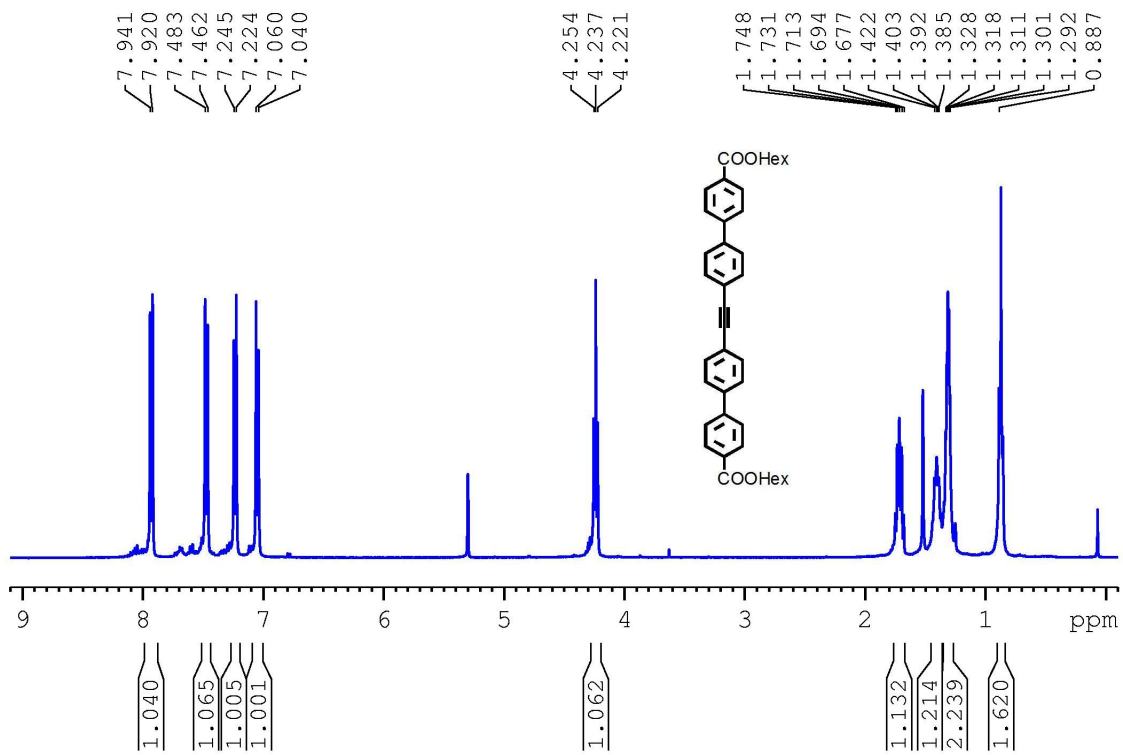
Synthesis of 4. This compound was prepared by a previously reported procedure with slight modification²¹. Under an argon atmosphere, hexabromobenzene (150 mg, 0.27 mmol), **3**²² (380 mg, 2.18 mmol), Pd(PPh₃)₂Cl₂ (19 mg, 0.027 mmol), CuI (10 mg, 0.054 mmol), PPh₃ (14 mg, 0.54 mmol), and degassed Et₃N (15 mL) were combined in a 50 mL two neck round bottom flask. This mixture was stirred at refluxing temperature for 48 h. After removal of organic solvent, the crude product was purified by column chromatography on silica gel with CH₂Cl₂/ethyl acetate (EA) (2:1 v/v) to give compound **4** as a yellow solid. Yield: 208 mg, 69%. ¹H NMR (CDCl₃, 400 MHz): δ 8.04 (d, *J* = 8.2 Hz, 12H), 7.63 (d, *J* = 8.2 Hz, 12H), 4.42 (q, *J* = 7.1 Hz, 12H), 1.43 (t, *J* = 7.1 Hz, 18H).

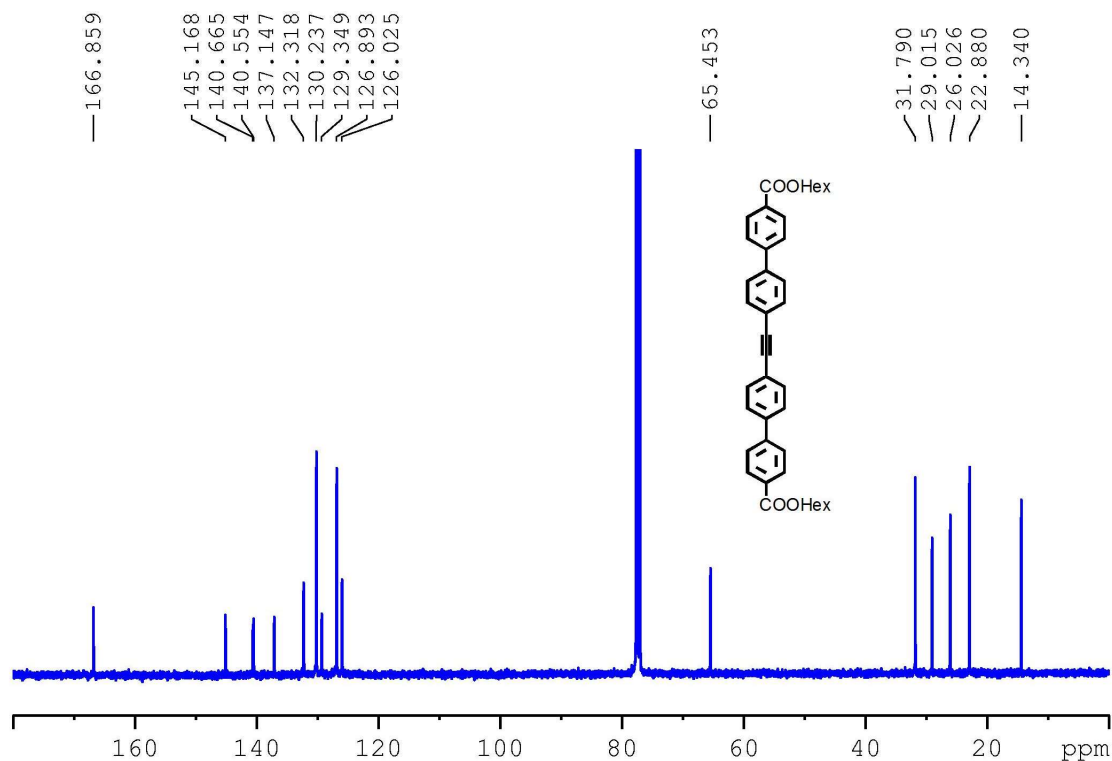
Synthesis of hexakis(4-carboxyphenylethynyl)benzene (5 = H₆L1). Under an argon atmosphere, a solution of compound **4** (200 mg, 0.18 mmol) in THF (15 mL) was added to a

solution of KOH (840 mg, 15 mmol) in H₂O (15 mL). The suspension mixture was stirred at 70 °C for 48 h. After removal of organic solvent, the aqueous residue was acidified with 2 M HCl. The resulting precipitate was filtered, washed with H₂O, and dried under vacuum to afford **5 (H₆L1)** as a dark yellow solid. Yield: 152 mg, 90%. ¹H NMR (DMSO, 400 MHz): δ 13.12 (s, 6H), 7.76 (d, *J* = 7.6 Hz, 12H), 7.41 (d, *J* = 7.7 Hz, 12H).

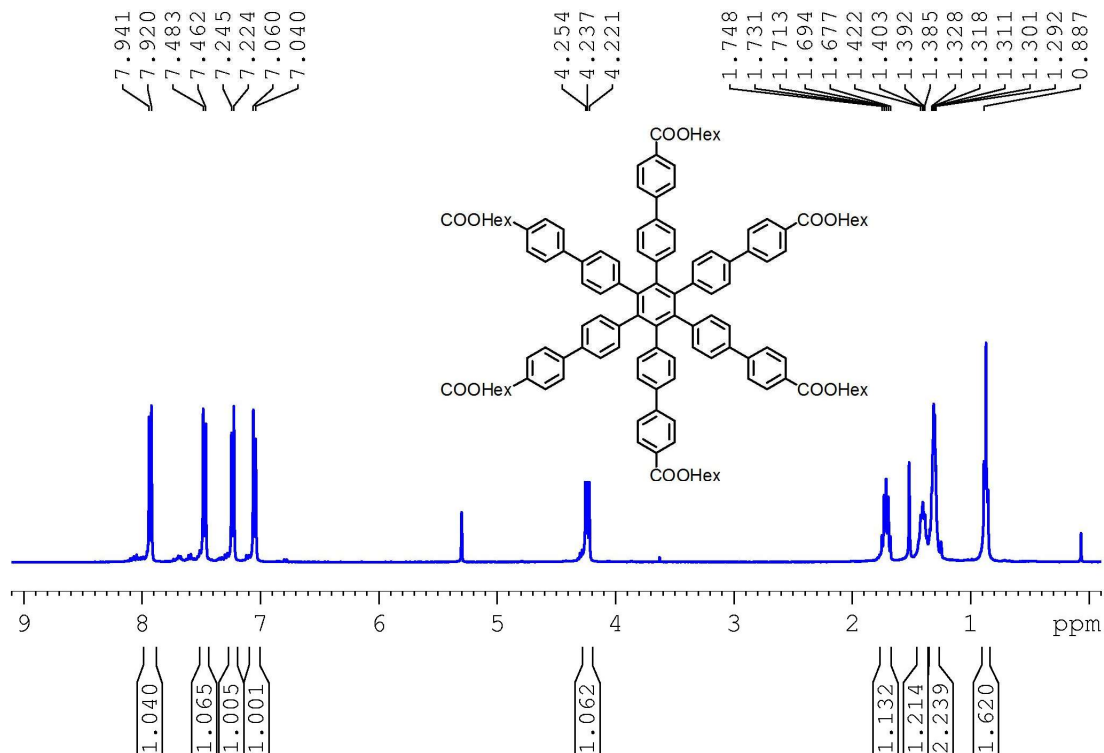
Synthesis of 10. Under an argon atmosphere, compound **9**²³ (2.85 g, 10 mmol), bis(pinacolato)diboron (2.8 g, 11 mmol), Pd(PPh₃)₂Cl₂ (0.18 g, 0.25 mmol), KOAc (2.95 g, 30 mmol), and degassed DME (40 mL) were combined in a 100 mL two neck round bottom flask. This mixture was stirred at refluxing temperature overnight. After removal of organic solvent, the crude product was purified by column chromatography on silica gel with CH₂Cl₂/hexanes (1:1 v/v) to give compound **10** as colorless oil. Yield: 2.66 g, 80%. ¹H NMR (CDCl₃, 300 MHz): δ 8.02 (d, *J* = 8.2 Hz, 2H), 7.86 (d, *J* = 8.2 Hz, 2H), 4.31 (t, *J* = 6.7 Hz, 2H), 1.69-1.84 (m, 2H), 1.36 (s, 12H), 1.28-1.50 (m, 6H), 0.90 (t, *J* = 6.7 Hz, 3H). ¹³C NMR (CDCl₃, 100 MHz): δ 135.0, 133.0, 128.9, 84.5, 65.5, 53.7, 31.8, 29.0, 26.0, 25.2, 22.9, 14.3.

Synthesis of 11. Under an argon atmosphere, compound **8**²⁴ (1.00 g, 3.0 mmol), compound **10** (2.1 g, 6.3 mmol), Pd(PPh₃)₄ (0.18 g, 1.5 mmol), and Na₂CO₃ (0.95 g, 9.0 mmol) were combined in a 100 mL two neck round bottom flask. To this 60 mL of degassed solvent mixture of toluene-methanol-water (2:1:1 v/v) was added. After the reaction mixture was stirred at refluxing temperature for 48 h, this solution was concentrated and extracted with CH₂Cl₂ (30 mL × 3). The organic phase was washed for three times with brine solution and dried with anhydrous Mg₂SO₄. The filtered solutions was concentrated under reduce pressure. And the crude product was purified by column chromatography on silica gel with CH₂Cl₂/hexanes (3:2 v/v) to give compound **11** as a white solid. Yield: 1.13 g, 65%. ¹H NMR (CDCl₃, 400 MHz): δ 8.13 (d, *J* = 8.3 Hz, 4H), 7.68 (d, *J* = 8.3 Hz, 4H), 7.64 (s, 8H), 4.35 (t, *J* = 6.6 Hz, 4H), 1.72-1.86 (m, 4H), 1.29-1.52 (m, 12H), 0.92 (t, *J* = 6.9 Hz, 6H). ¹³C NMR (CDCl₃, 100 MHz): δ 166.9, 145.2, 146.7, 140.6, 137.1, 132.3, 130.2, 129.3, 126.9, 126.0, 65.5, 31.8, 29.0, 26.0, 22.9, 14.3.

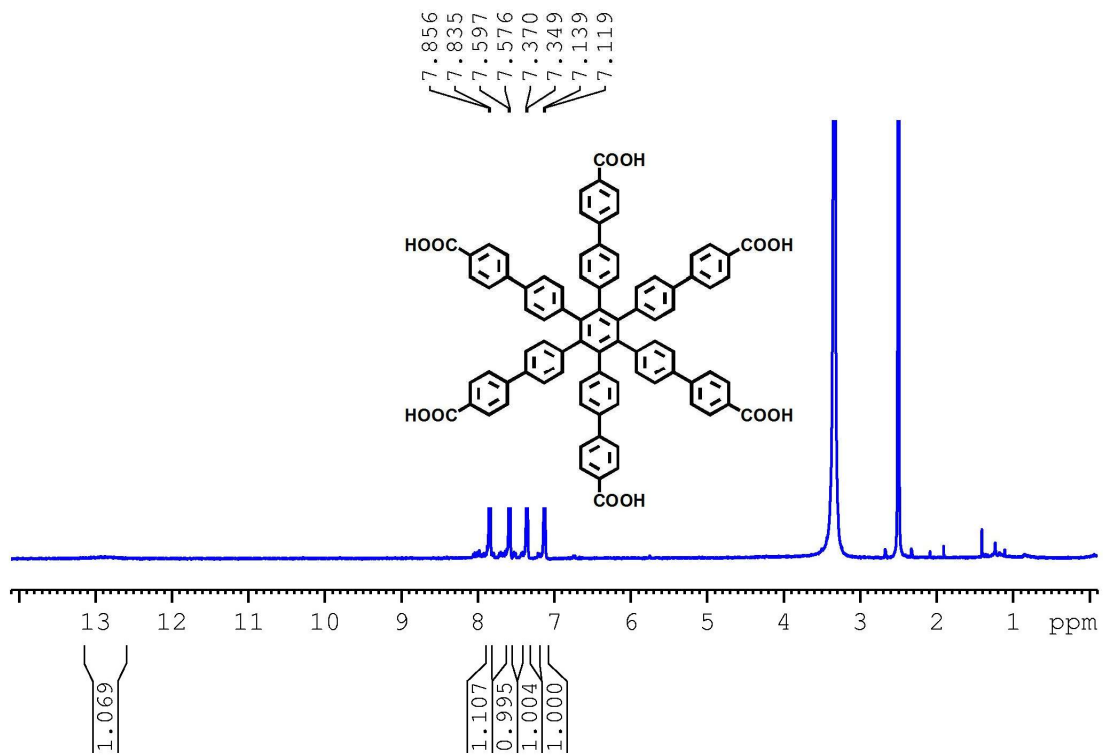


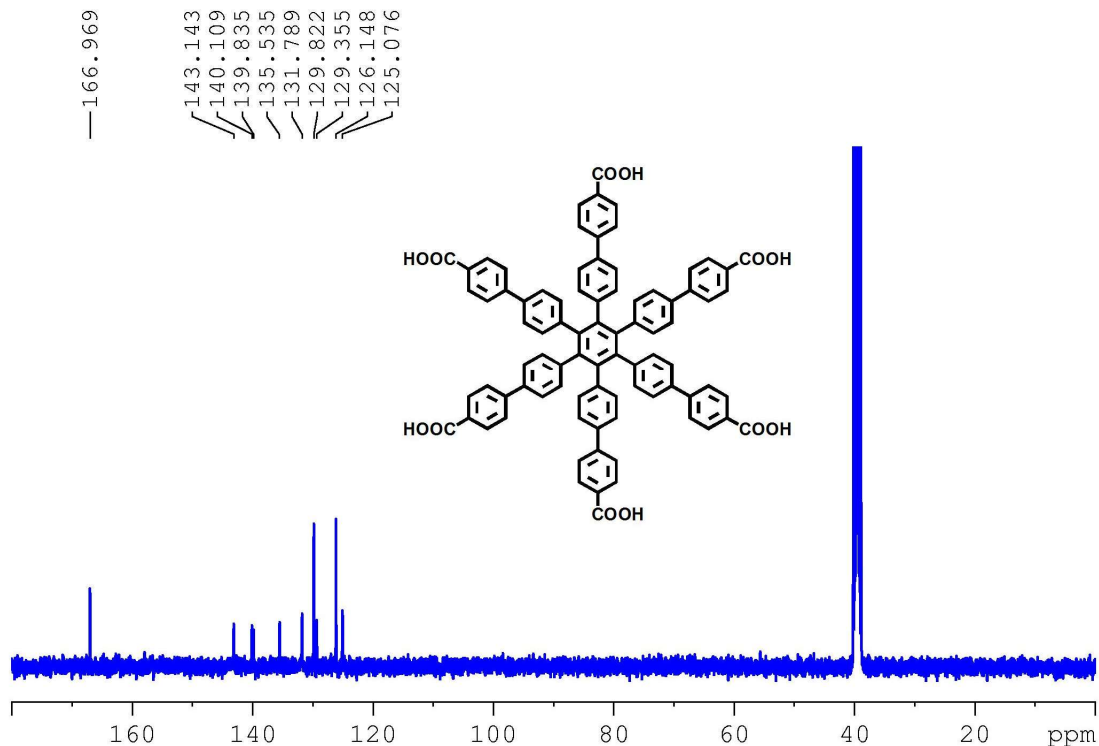


Synthesis of 12. Under an argon atmosphere, compound **11** (1.0 g, 1.7 mmol), $\text{Co}_2(\text{CO})_8$ (0.2 g, 0.57 mmol), and degassed dioxane (50 mL) were combined in a 100 mL two neck round bottom flask. This mixture was stirred at refluxing temperature for 72 h. After removal of organic solvent, the crude product was purified by column chromatography on silica gel with $\text{CH}_2\text{Cl}_2/\text{EA}$ (5:1 v/v) to give compound **12** as a white solid. Yield: 0.68 g, 68%. ¹H NMR (CD_2Cl_2 , 400 MHz): δ 7.94 (d, $J = 8.4$ Hz, 12H), 7.48 (d, $J = 8.4$ Hz, 12H), 7.24 (d, $J = 8.3$ Hz, 12H), 7.06 (d, $J = 8.3$ Hz, 12H), 4.25 (t, $J = 6.7$ Hz, 12H), 1.65-1.82 (m, 12H), 1.22-1.49 (m, 36 H), 0.88 (t, $J = 7.0$ Hz, 18H).

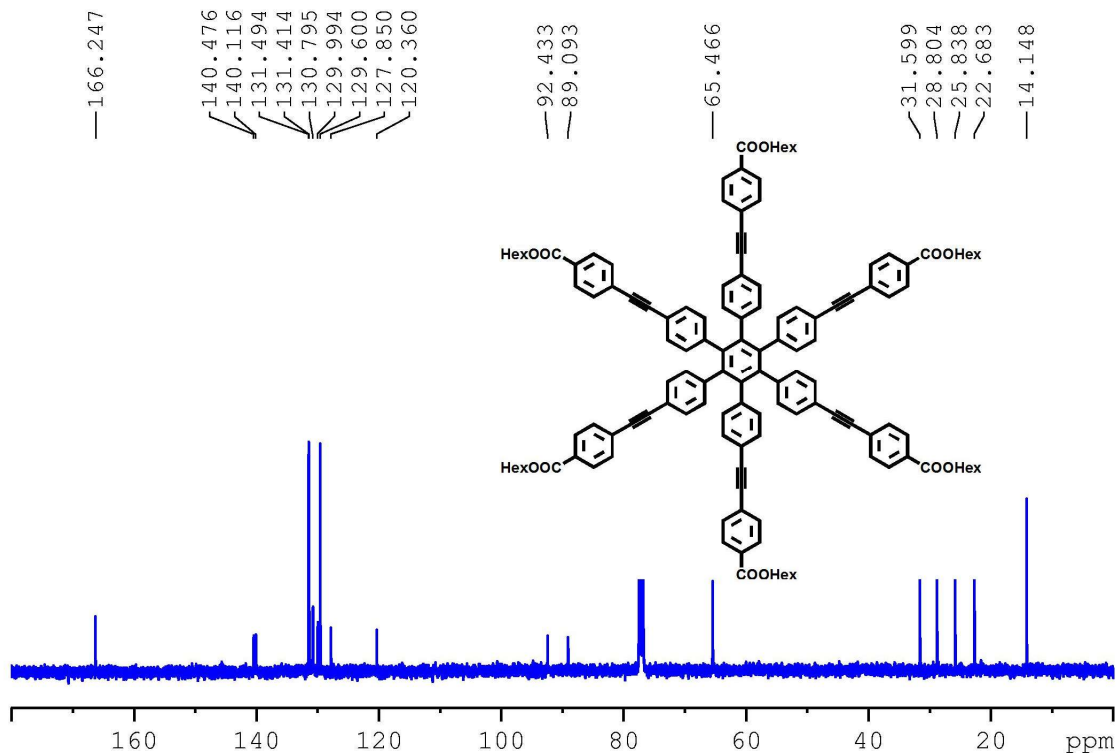


Synthesis of hexakis(4-(4-carboxylphenyl)phenyl)benzene (13** = **H₆L2**).** Under an argon atmosphere, a solution of compound **12** (600 mg, 0.34 mmol) in THF (30 mL) was added to a solution of KOH (1.68 g, 30 mmol) in H₂O (30 mL). The suspension mixture was stirred at refluxing temperature for 72 h. After removal of organic solvent, the aqueous residue was acidified with 2 M HCl. The resulting precipitate was filtered, washed with H₂O, and dried under vacuum to afford **13** (**H₆L2**) as a light yellow solid. Yield: 400 mg, 94%. ¹H NMR (DMSO, 400 MHz): δ 13.10 (s, 6H), 7.85 (d, *J* = 8.5 Hz, 12H), 7.59 (d, *J* = 8.5 Hz, 12H), 7.36 (d, *J* = 8.4 Hz, 12H), 7.13 (d, *J* = 8.2 Hz, 12H). ¹³C NMR (DMSO, 100 MHz): δ 167.0, 143.1, 140.1, 139.8, 135.5, 131.8, 129.8, 129.4, 126.1, 125.1.





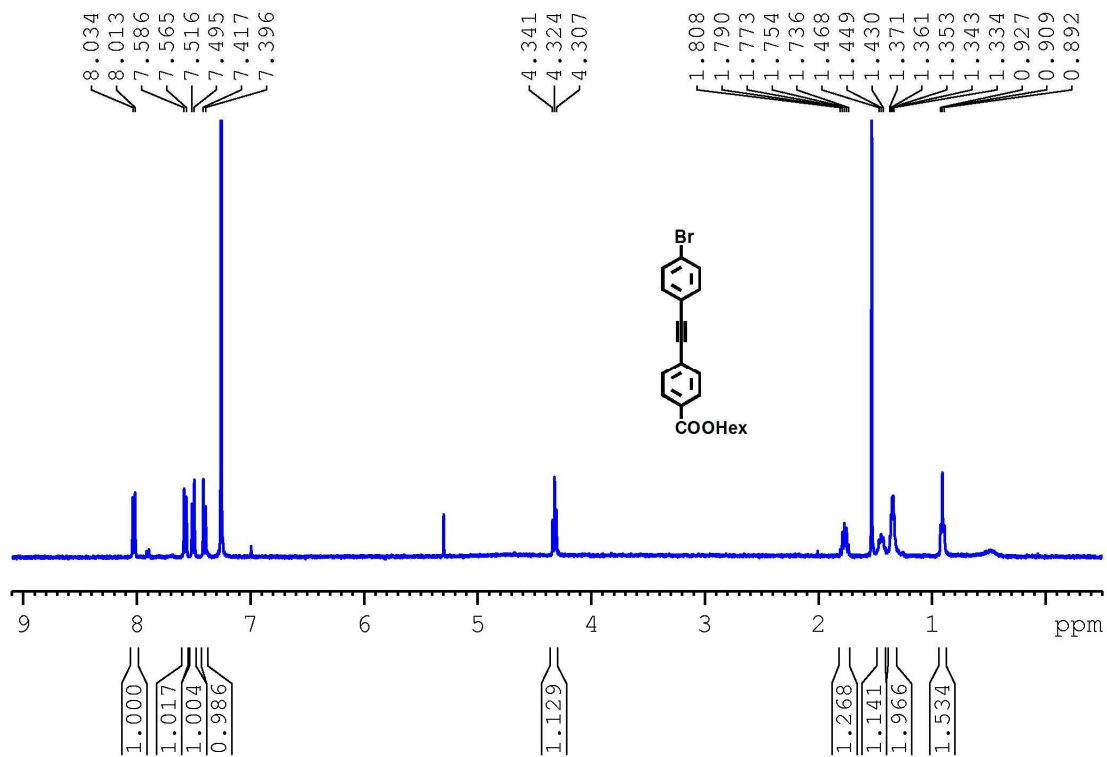
Synthesis of 18. Under an argon atmosphere, compound **15**²⁵ (150 mg, 0.12 mmol), compound **17**²⁶ (220 mg, 0.96 mmol), Pd(PPh₃)₂Cl₂ (17 mg, 0.024 mmol), CuI (4.5 mg, 0.024 mmol), and degassed solvent mixture of Et₃N (5 mL) and THF (25 mL) were combined in a 50mL two neck round bottom flask. This mixture was stirred at 50 °C for 72 h. After removal of organic solvent, the crude product was purified by column chromatography on silica gel with CH₂Cl₂/EA (10:1 v/v) to give compound **18** as a yellow solid. Yield: 148 mg, 45%. ¹H NMR (CDCl₃, 400 MHz): δ 7.97 (d, *J* = 8.5 Hz, 12H), 7.49 (d, *J* = 8.5 Hz, 12H), 7.14 (d, *J* = 8.3 Hz, 12H), 6.84 (d, *J* = 8.3 Hz, 12H), 4.30 (t, *J* = 6.7 Hz, 12H), 1.68-1.81 (m, 12H), 1.25-1.49 (m, 36H), 0.89 (t, *J* = 7.0 Hz, 18H). ¹³C NMR (CDCl₃, 100 MHz): δ 166.2, 140.5, 140.1, 131.5, 131.4, 130.8, 130.0, 129.6, 127.8, 120.4, 92.4, 89.1, 65.5, 31.6, 28.8, 25.8, 22.7, 14.1.

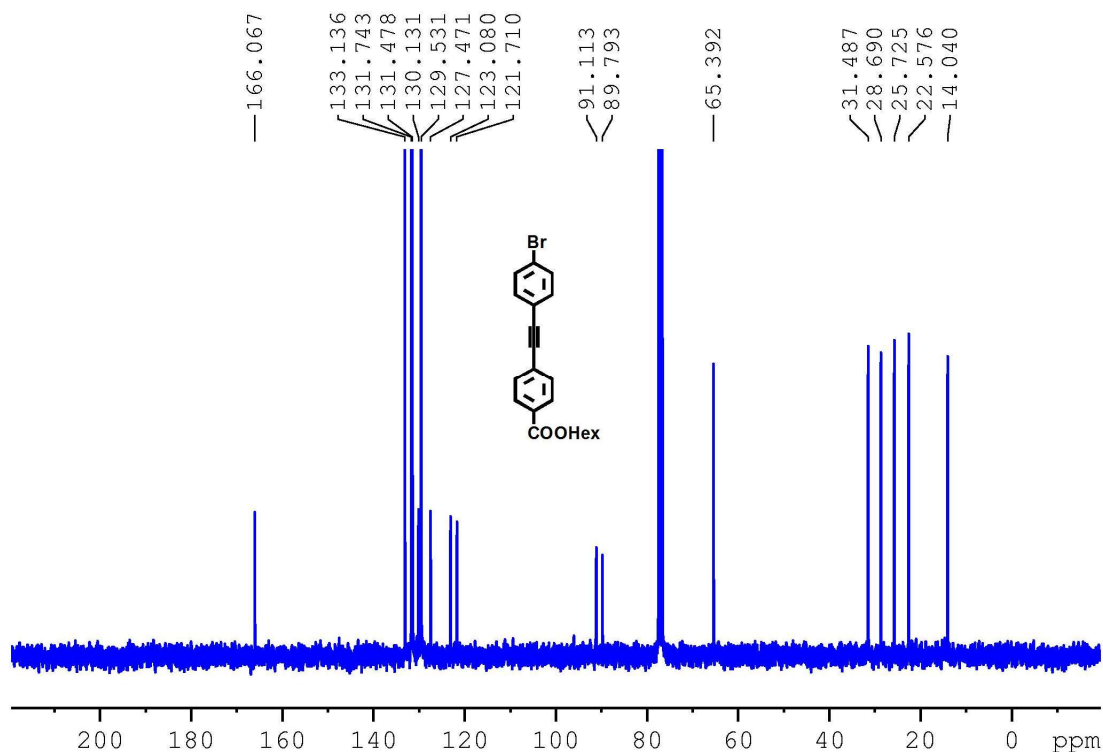


Synthesis of hexakis(4-(4-carboxylphenylethynyl)phenyl)benzene (19 = H₆L3). Under an argon atmosphere, a solution of compound **18** (140 mg, 0.074 mmol) in THF (20 mL) was added to a solution of KOH (1.12 g, 20 mmol) in H₂O (20 mL). The suspension mixture was stirred at refluxing temperature for 72 h. After removal of organic solvent, the aqueous residue was acidified with 2 M HCl. The resulting precipitate was filtered, washed with H₂O, and dried under vacuum to afford **19** (H₆L3) as a light yellow solid. Yield: 92 mg, 90%. ¹H NMR (DMSO, 400 MHz): δ 13.09 (s, 6H), 7.91 (d, *J* = 8.4 Hz, 12H), 7.60 (d, *J* = 8.4 Hz, 12H), 7.20 (d, *J* = 8.2 Hz, 12 H), 7.01 (d, *J* = 8.3 Hz, 12 H), ¹³C NMR (DMSO, 100 MHz): δ 167.3, 141.2, 140.9, 132.3, 132.0, 131.1, 130.8, 130.2, 128.3, 121.2, 92.6, 89.4.

Synthesis of 20. Under an argon atmosphere, compound **17**²⁶ (1.15 g, 5 mmol), 1-bromo-4-iodobenzene (1.42 g, 5 mmol), Pd(PPh₃)₂Cl₂ (175 mg, 0.25 mmol), CuI (48 mg, 0.5 mmol), and degassed solvent mixture of Et₃N (5 mL) and THF (45 mL) were combined in a 100mL two neck round bottom flask. This mixture was stirred at room temperature for overnight. After removal of organic solvent, the crude product was purified by column chromatography on silica gel with CH₂Cl₂/hexanes (1:2 v/v) to give compound **20** as a white solid. Yield: 1.73 g, 90%. ¹H NMR (CDCl₃, 400 MHz): δ 8.02 (d, *J* = 8.3 Hz, 2H), 7.58 (d, *J* = 8.2 Hz, 2H), 7.51 (d, *J* = 8.6 Hz, 2H), 7.41 (d, *J* = 8.6 Hz, 2H), 4.32 (t, *J* = 6.7 Hz, 2H), 1.68-1.81 (m, 2H), 1.25-1.49 (m, 6H), 0.91 (t,

$J = 6.9$ Hz, 3H). ^{13}C NMR (CDCl_3 , 100 MHz): δ 166.1, 133.1, 131.7, 131.5, 130.1, 129.5, 127.5, 123.1, 121.7, 91.1, 89.8, 65.4, 31.5, 28.7, 25.7, 22.6, 14.0.



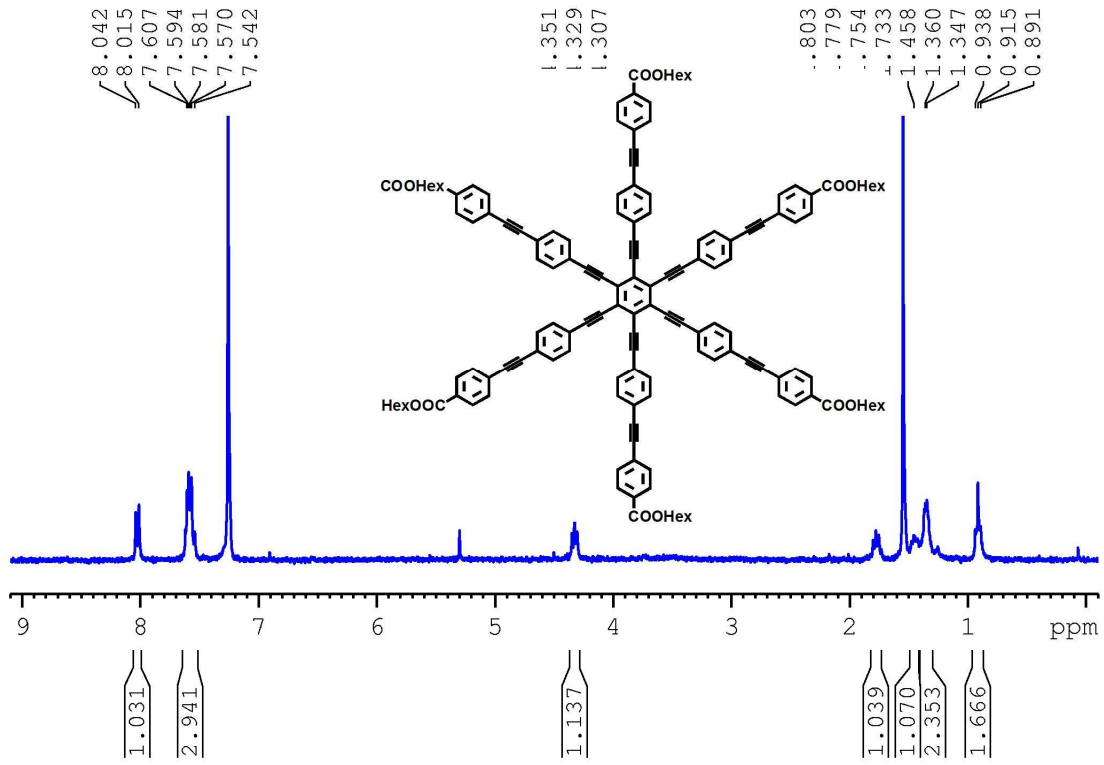


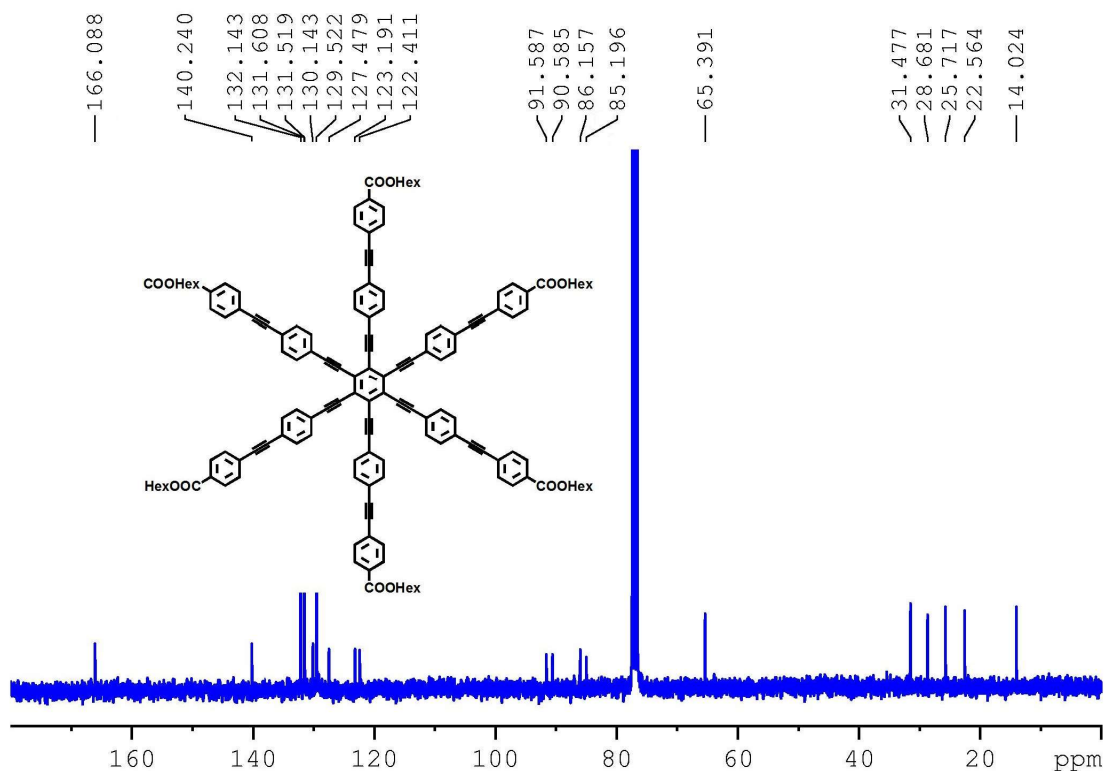
Synthesis of 21. Under an argon atmosphere, compound **20** (1.7 g, 4.4 mmol), trimethylsilylacetylene (650 mg, 6.6 mmol), Pd(PPh₃)₂Cl₂ (155 mg, 0.22 mmol), CuI (42 mg, 0.22 mmol), and degassed solvent mixture of Et₃N (5 mL) and THF (45 mL) were combined in a 100mL two neck round bottom flask. This mixture was stirred at refluxing temperature for 48 h. After removal of organic solvent, the crude product was purified by column chromatography on silica gel with CH₂Cl₂/hexanes (1:2 v/v) to give compound **21** as a white solid. Yield: 1.38 g, 78%. ¹H NMR (CDCl₃, 400 MHz): δ 8.02 (d, *J* = 8.3 Hz, 2H), 7.57 (d, *J* = 8.2 Hz, 2H), 7.47 (d, *J* = 8.6 Hz, 2H), 7.45 (d, *J* = 8.6 Hz, 2H), 4.32 (t, *J* = 6.7 Hz, 2H), 1.71-1.82 (m, 2H), 1.27-1.50 (m, 6H), 0.91 (t, *J* = 6.9 Hz, 3H), 0.26 (s, 9H).

Synthesis of 22. To a solution of compound **21** (1.3 g, 3.2 mmol) in CH₂Cl₂ (40 mL), a 1 M solution of *n*-Bu₄N⁺F⁻ in THF (4 mL, 4 mmol) was added. The mixture was stirred at room temperature for 15 minutes and concentrated to dryness. The crude product was purified by a short column chromatography on silica gel with CH₂Cl₂ as eluent to give compound **22** as a white solid. Yield: 868 mg, 82%. ¹H NMR (CDCl₃, 400 MHz): δ 8.03 (d, *J* = 8.3 Hz, 2H), 7.58 (d, *J* = 8.3 Hz, 2H), 7.49 (d, *J* = 8.6 Hz, 2H), 7.47 (d, *J* = 8.6 Hz, 2H), 4.32 (t, *J* = 6.7 Hz, 2H), 3.20 (s, 2H), 1.70-1.82 (m, 2H), 1.25-1.49 (m, 6H), 0.91 (t, *J* = 7.0 Hz, 3H).

Synthesis of 23. Under an argon atmosphere, hexabromobenzene (100 mg, 0.18 mmol), compound **22** (480 mg, 1.44 mmol), Pd(PPh₃)₂Cl₂ (13 mg, 0.018 mmol), CuI (7 mg, 0.036

mmol), solvent mixture of Et₃N (5 mL) and THF (45 mL) were combined in a 100mL two neck round bottom flask. This mixture was stirred at refluxing temperature for 72 h. After removal of organic solvent, the crude product was purified by column chromatography on silica gel with CH₂Cl₂/EA (5:1 v/v) to give compound **23** as a yellow solid. Yield: 122 mg, 33%. ¹H NMR (CDCl₃, 400 MHz): δ 8.03 (d, *J* = 8.1 Hz, 12H), 7.65-7.50 (m, 36H), 4.33 (t, *J* = 6.7 Hz, 12H), 1.68-1.81 (m, 12H), 1.25-1.49 (m, 36H), 0.91 (t, *J* = 6.9 Hz, 18H). ¹³C NMR (CDCl₃, 100 MHz): δ 166.1, 140.2, 132.1, 131.6, 131.5, 130.1, 130.0, 129.5, 127.5, 123.2, 122.4, 91.6, 90.6, 86.2, 85.2, 65.4, 28.7, 25.7, 22.5, 14.0.





Synthesis of hexakis(4-(4-carboxyphenylethynyl)phenylethynyl)benzene (24** = **H₆L4**).** Under an argon atmosphere, a solution of compound **23** (110 mg, 0.054 mmol) in THF (20 mL) was added to a solution of KOH (1.12 g, 20 mmol) in H₂O (20 mL). The suspension mixture was stirred at refluxing temperature for 72 h. After removal of organic solvent, the aqueous residue was acidified with 2 M HCl. The resulting precipitate was filtered, washed with H₂O, and dried under vacuum to afford **19** (**H₆L3**) as a dark yellow solid. Yield: 75 mg, 91%.

Synthesis of she-MOF-1. H₆L1 (20 mg, 0.021 mmol) and Cu(NO₃)₂·3H₂O (20.5 mg, 0.0848 mmol) were dissolved in 20 mL of DMF and DMSO (v/v=1:1) in a vial, to which acetic acid (0.8 mL) were added. The vial was tightly capped and placed in a 80 °C oven for 84 h to yield 12.3 mg of green polyhedral crystals (yield: 49% based on H₆L1). Activation procedure: the supernatant was decanted and fresh acetone was added for the solvent exchange. The crystals were soaked in acetone for 12 h after which the supernatant was decanted. This process was repeated 3 times with soaking time of 12 h. Then, the crystals of she-MOF-1 were transferred into a sorption tube with acetone. When the solid settled down in the tube, the acetone was decanted and the tube was attached to SmartVacPrep. (Micromeritics, GA). The sample was first outgassed at 1 mm Hg/s and the vacuum is unrestricted when the pressure reach 5 mm Hg. The sample was heated at 40 °C for 2 h and then 50 °C for 2 h, and the temperature is held at 60 °C for 12 h.

Synthesis of she-MOF-2. H₆L2 (20 mg, 0.016 mmol) and Cu(NO₃)₂·3H₂O (15.4 mg, 0.0637 mmol) were dissolved in 20 mL of DMF in a vial, to which acetic acid (0.8 mL) were added. The vial was tightly capped and placed in a 80 °C oven for 72 h to yield 13.5 mg of green polyhedral crystals (yield: 57% based on H₆L2). Activation procedure: fresh absolute ethanol was used to exchange the DMF molecules, which was repeated three times over three days. This crystals were subjected to supercritical carbon dioxide drying reported in previous paper.^{27, 28} Liquid CO₂ was used to exchange the ethanol, the system was vented 5 times over the course of 10 hours to fully exchange the ethanol with CO₂. The system was then bled at the rate of 0.2 mL/s. Subsequently the samples were transferred into a sorption tube in a glovebox and dried on an activation port of an ASAP 2020 (Micromeritics, GA) under dynamic vacuum at 30 °C for 12 h.

Synthesis of she-MOF-3. H₆L3 (20 mg, 0.014 mmol) and Cu(NO₃)₂·3H₂O (150 mg, 6.45 × 10⁻⁴ mol) were dissolved in 15 mL of N,N-dimethylformamide (DMF) in a vial, to which acetic acid (0.8 mL) were added. The vial was tightly capped and placed in a 80 °C oven for 72 h to yield 9.6 mg of green polyhedral crystals (yield: 41% based on H₆L3).

Synthesis of she-MOF-4. H₆L4 (20 mg, 0.013 mmol) and Cu(NO₃)₂·3H₂O (13 mg, 0.052 mmol) were dissolved in 20 mL of DMF in a vial, to which acetic acid (0.8 mL) were added. The vial was tightly capped and placed in a 80 °C oven for 72 h to yield 5.3 mg of green polyhedral crystals (yield: 23% based on H₆L4).

Synthesis of NU-1103. The sample of **NU-1103** was synthesized two years ago. The procedure for the synthesis of this MOF is described in detail in ref. 2.

Section S7. Single crystal X-ray structure determination

Single crystal X-ray diffraction data was collected using synchrotron radiation at the Advanced Photon Source, Chicago, IL. Indexing was performed using APEX2 (Difference Vectors method).²⁹ Data integration and reduction were performed using SaintPlus 6.01.³⁰ Absorption correction was performed by multi-scan method implemented in SADABS.³¹ Space groups were determined using XPREP implemented in APEX2.²⁹ The structure was solved using SHELXS-2013 (Patterson method) and refined using SHELXL-2013 (full-matrix least-squares on F^2) contained in APEX2 and WinGX v1.70.00.³²⁻³⁵ C,N,O atoms were refined with anisotropic displacement parameters and H atoms were placed in geometrically calculated positions and included in the refinement process using riding model with isotropic thermal parameters: $U_{\text{iso}}(\text{H}) = 1.2U_{\text{eq}}(-\text{CH})$. The contribution of disordered solvent molecules was treated as diffuse using the SQUEEZE procedure implemented in PLATON.³⁶ Crystal data and refinement conditions are shown in Table S5-S7. CCDC 1415756, 1415757, 1415758 contains the supplementary crystallographic data for this paper. This data can be obtained free of charge from The Cambridge Crystallographic Data Centre via www.ccdc.cam.ac.uk/data_request/cif.

Table S6. Crystal data and structure refinement for **she-MOF-1**.

Empirical formula	C ₆₀ H ₂₄ Cu ₃ O ₁₅
Formula weight (g/mol)	1175.41
Temperature (K)	296(2)
Wavelength (Å)	0.41328
Crystal system	cubic
Space group	<i>I</i> m-3m
a (Å)	34.600
Volume (Å ³)	41424(38)
Z	8
Density (g·cm ⁻³)	0.377
Absorption coefficient (mm ⁻¹)	0.076
F(000)	4728
Crystal size (mm ³)	0.28 × 0.28 × 0.18 mm
θ range (deg)	1.18 to 28.64 deg
Reflections collected	143569
Independent reflections	4941
Completeness (%)	99.3
Refinement method	Full-matrix least-squares on F^2
Data / parameters / restraints	4941 / 67 / 0
Goodness-of-fit on F^2	1.118
Final R indices [$I > 2\sigma(I)$]	$R_1 = 0.0608$, $wR_2 = 0.2237$
Largest diff. peak and hole (e ⁻ ·Å ⁻³)	1.057 and -0.398

Table S7. Crystal data and structure refinement for **she-MOF-2**.

Empirical formula	C ₈₄ H ₄₈ Cu ₃ O ₁₅
Formula weight (g/mol)	1487.84
Temperature (K)	296(2)
Wavelength (Å)	0.44280
Crystal system	cubic
Space group	<i>I</i> m-3m
a (Å)	39.618(3)
Volume (Å ³)	62184(9)
Z	8
Density (g·cm ⁻³)	0.318
Absorption coefficient (mm ⁻¹)	0.062
F(000)	6072
Crystal size (mm ³)	0.25 × 0.25 × 0.20 mm
θ range (deg)	0.91 to 16.17 deg
Reflections collected	266732
Independent reflections	5887
Completeness (%)	98.0
Refinement method	Full-matrix least-squares on <i>F</i> ²
Data / parameters / restraints	5887 / 85 / 6
Goodness-of-fit on <i>F</i> ²	1.134
Final <i>R</i> indices [<i>I</i> >2σ(<i>I</i>)]	<i>R</i> ₁ = 0.1388, <i>wR</i> ₂ = 0.3607
Largest diff. peak and hole (e·Å ⁻³)	1.194 and -1.122

Table S8. Crystal data and structure refinement for **she-MOF-3**.

Empirical formula	C ₉₆ H ₄₈ Cu ₃ O ₁₅
Formula weight (g/mol)	1631.96
Temperature (K)	296(2)
Wavelength (Å)	0.41328
Crystal system	cubic
Space group	<i>I</i> m-3m
a (Å)	46.744(3)
Volume (Å ³)	102136(12)
Z	8
Density (g·cm ⁻³)	0.212
Absorption coefficient (mm ⁻¹)	0.032
F(000)	6648
Crystal size (mm ³)	0.15 × 0.15 × 0.12 mm
θ range (deg)	1.13 to 14.97 deg
Reflections collected	380903
Independent reflections	9109
Completeness (%)	95.4
Refinement method	Full-matrix least-squares on <i>F</i> ²
Data / parameters / restraints	9109 / 95 / 39
Goodness-of-fit on <i>F</i> ²	1.147
Final <i>R</i> indices [<i>I</i> >2σ(<i>I</i>)]	<i>R</i> ₁ = 0.1388, <i>wR</i> ₂ = 0.3556
Largest diff. peak and hole (e·Å ⁻³)	0.817 and -0.740

Section S8. TGA data

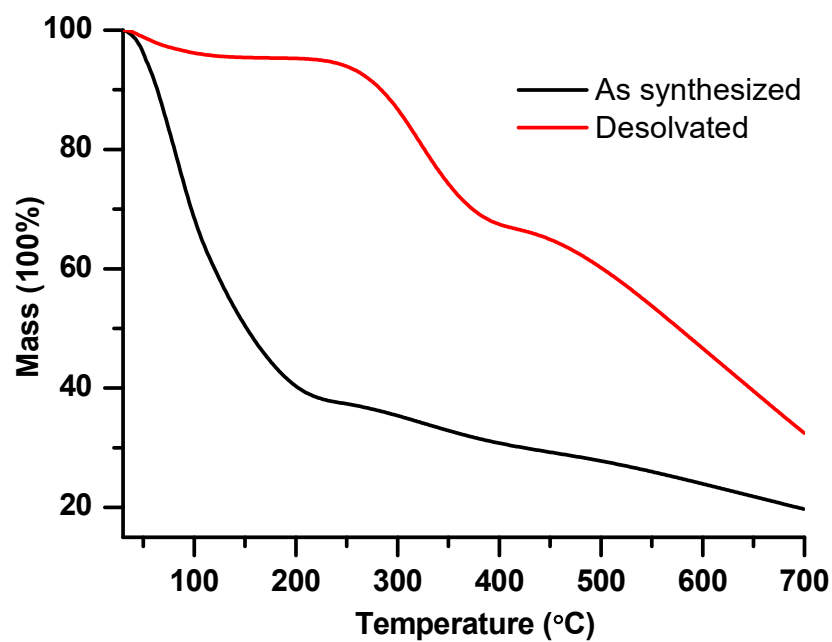


Figure S13. The TGA trace for she-MOF-1 (red: desolvated, black as synthesized).

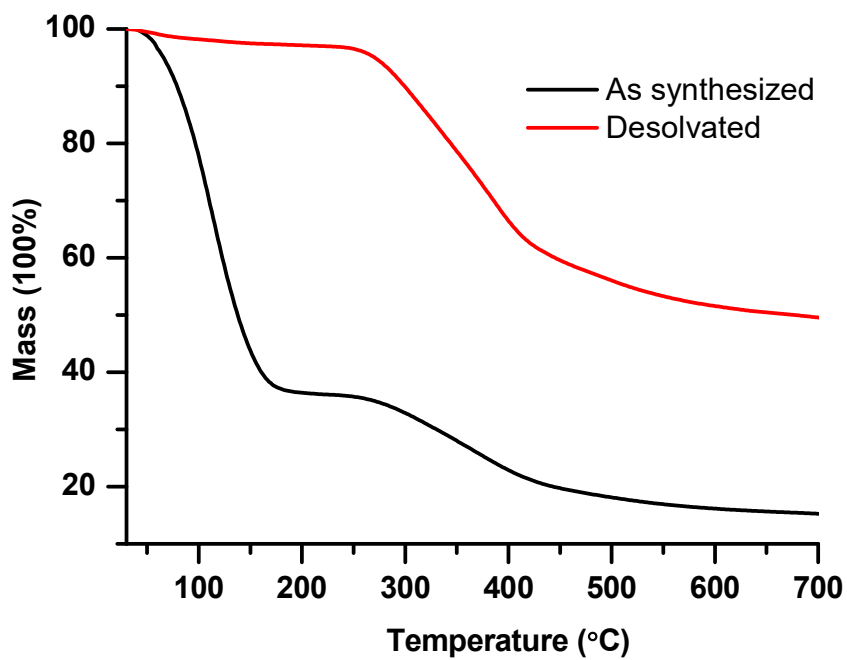


Figure S14. The TGA trace for she-MOF-2 (red: desolvated, black: as synthesized).

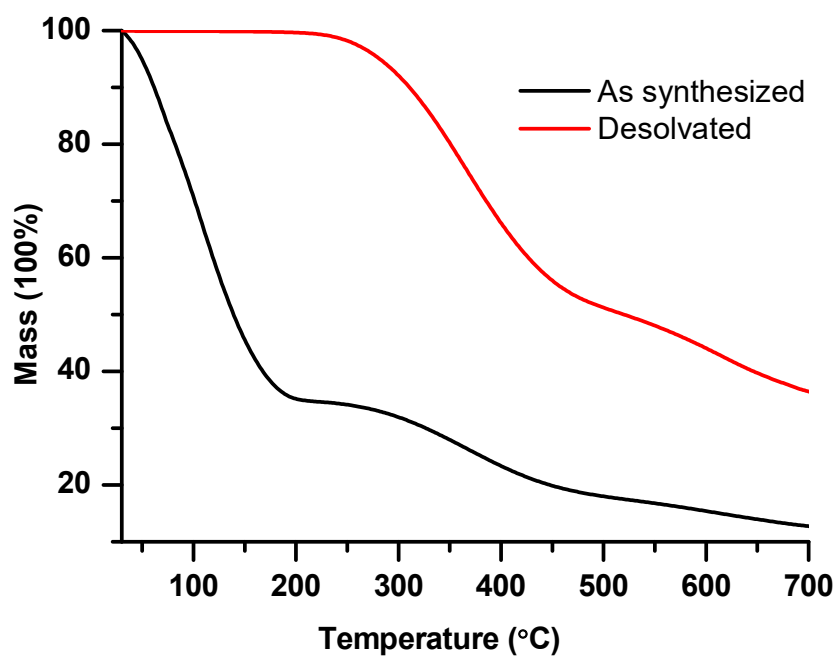


Figure S15. The TGA trace for she-MOF-3 (red: desolvated, black: as synthesized).

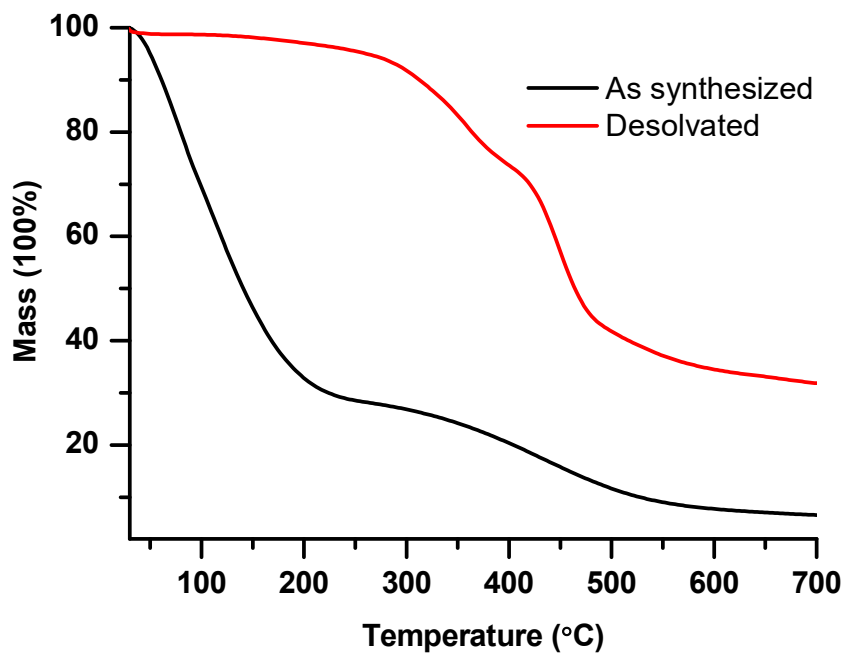


Figure S16. The TGA trace for she-MOF-4 (red: desolvated, black: as synthesized).

Section S9. MOF activation and surface area determination

Activation procedures:

she-MOF-1:

The DMF was decanted and fresh acetone was added for the solvent exchange. The sample was soaked in acetone for 12 h after which the supernatant was decanted. This process was repeated 3 times with soaking time of 12 h. Then, the sample was transferred into a sorption tube with acetone. When the solid settled down in the tube, the acetone was decanted and the tube was attached to SmartVacPrep. (Micromeritics, GA). The sample was first outgassed at 1 mm Hg/s and the vacuum is unrestricted when the pressure reached 5 mm Hg. The sample was heated at 40 °C for 2 h and then 50 °C for 2 h, and the temperature is held at 60 °C for 12 h.

she-MOF-2:

Fresh absolute ethanol was used to exchange the DMF molecules with ethanol. The solvent exchange was repeated three times over three days. This sample was subjected to supercritical carbon dioxide drying procedure reported in a previous paper.^{27, 28} Liquid CO₂ was used to exchange the ethanol, the system was vented 5 times over the course of 10 hours to fully exchange the ethanol with CO₂. The system was then bled at the rate of 0.2 cc/s. Subsequently the samples were transferred into a sorption tube in a glovebox and dried on an activation port of an ASAP 2020 (Micromeritics, GA) under dynamic vacuum at 30 °C for 12 h.

NU-1103

The sample of **NU-1103** was activated two years ago. The procedure for activating NU-1103 is described in detail in ref. 2.

Nitrogen adsorption measurements:

she-MOF-1:

The nitrogen isotherm of the activated sample was taken on an ASAP 2020 (Micromeritics, GA) and the temperature was held at 77 K with a liquid nitrogen bath.

she-MOF-2:

The nitrogen isotherm of the activated sample was taken on an Tristar II (Micromeritics, GA) and the temperature was held at 77 K with a liquid nitrogen bath.

NU-1103

The nitrogen isotherm of the activated sample was measured at NIST. This isotherm was measured using a computer controlled Sievert apparatus, described in more detail in **Section S10**.

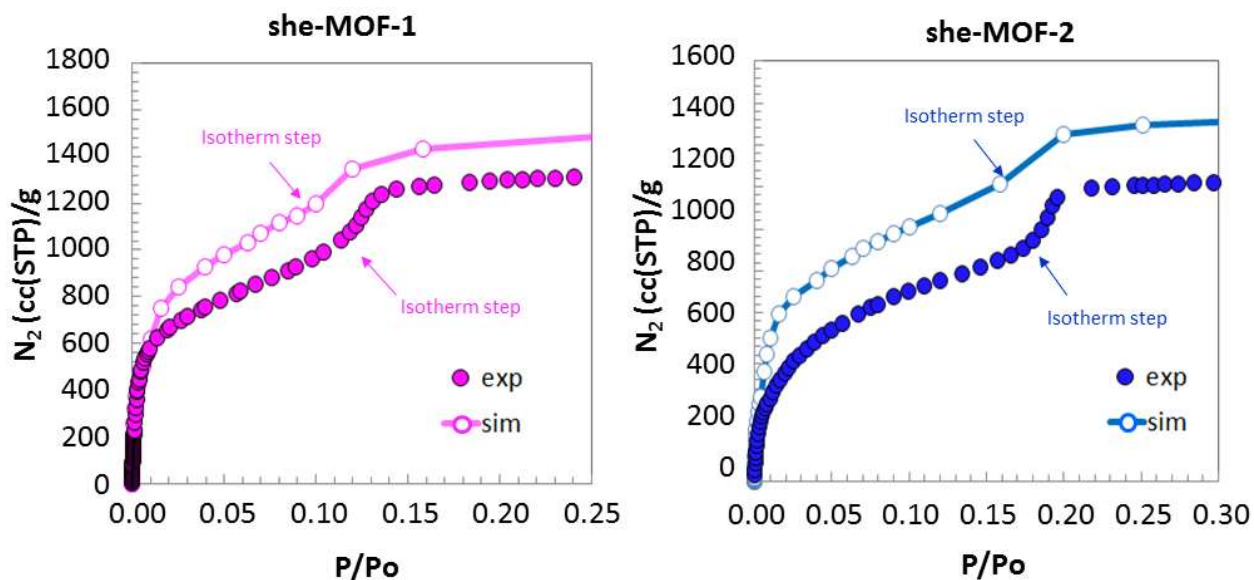


Figure S17. Close-up of the lower pressure region of simulated (white points) and measured (colored points) nitrogen isotherms of **she-MOF-1** and **she-MOF-2**.

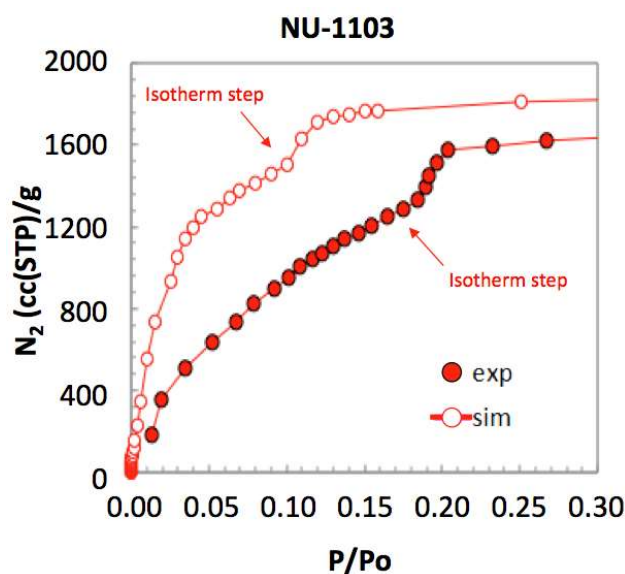


Figure S18. Close-up of the lower pressure regions of simulated (white points) and measured (colored points) nitrogen isotherm of **NU-1103**

Determination of MOF BET areas:

BET theory was applied to measured and simulated nitrogen isotherms for **she-MOF-1**, **she-MOF-2**, and **NU-1103** for estimation of MOF surface areas and assessment of sample quality after synthesis and activation. For a meaningful comparison between experimental and simulated BET areas, we applied the four consistency criteria suggested by Rouquerol *et al.*³⁷ as discussed in ref.² Figures S19-S21 show plots pertinent to the BET area calculation in **she-MOF-1**, **she-MOF-2** and **NU-1103**.

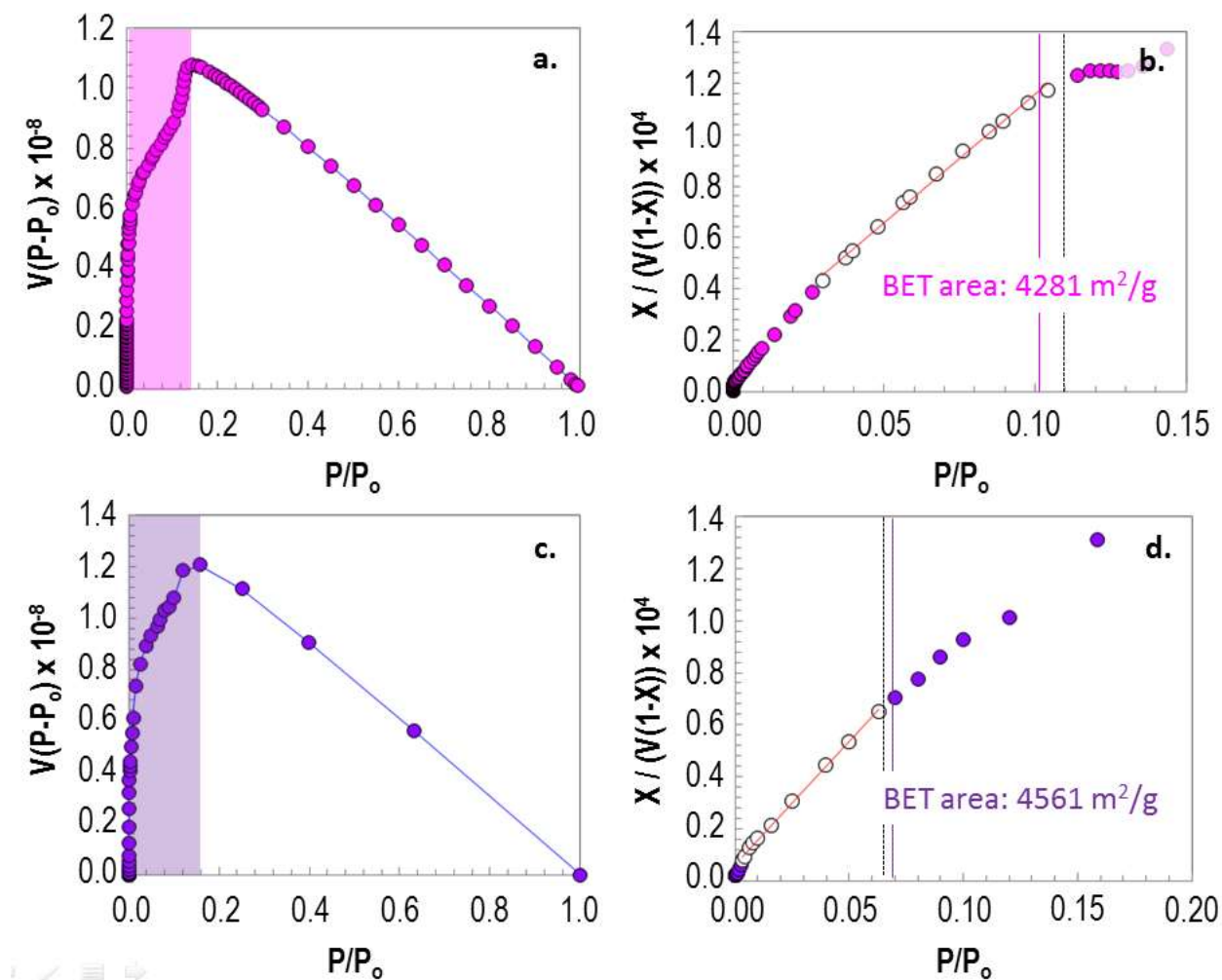


Figure S19. a-b) Plots for the determination of BET area of **she-MOF-1** from the experimental nitrogen isotherm. a) Plot to determine the region in which the first consistency criterion is fulfilled (region in pink). b) Plot to determine the BET region for the linear regression. Points used in the linear regression are shown in white. Pressure corresponding to the monolayer loading indicated by the vertical pink line. Pressure value obtained from $1/(\sqrt{C} + 1)$ indicated by the vertical dashed line. c-d) Plots for the determination of BET area of **she-MOF-1** from the simulated nitrogen isotherm. c) Plot to determine the region in which the first consistency criterion is fulfilled (region in purple). d) Plot to determine the BET region for the linear regression. Points used in the linear regression are shown in white. Pressure corresponding to the monolayer loading indicated by the vertical purple line. Pressure value obtained from $1/(\sqrt{C} + 1)$ indicated by the vertical dashed line.

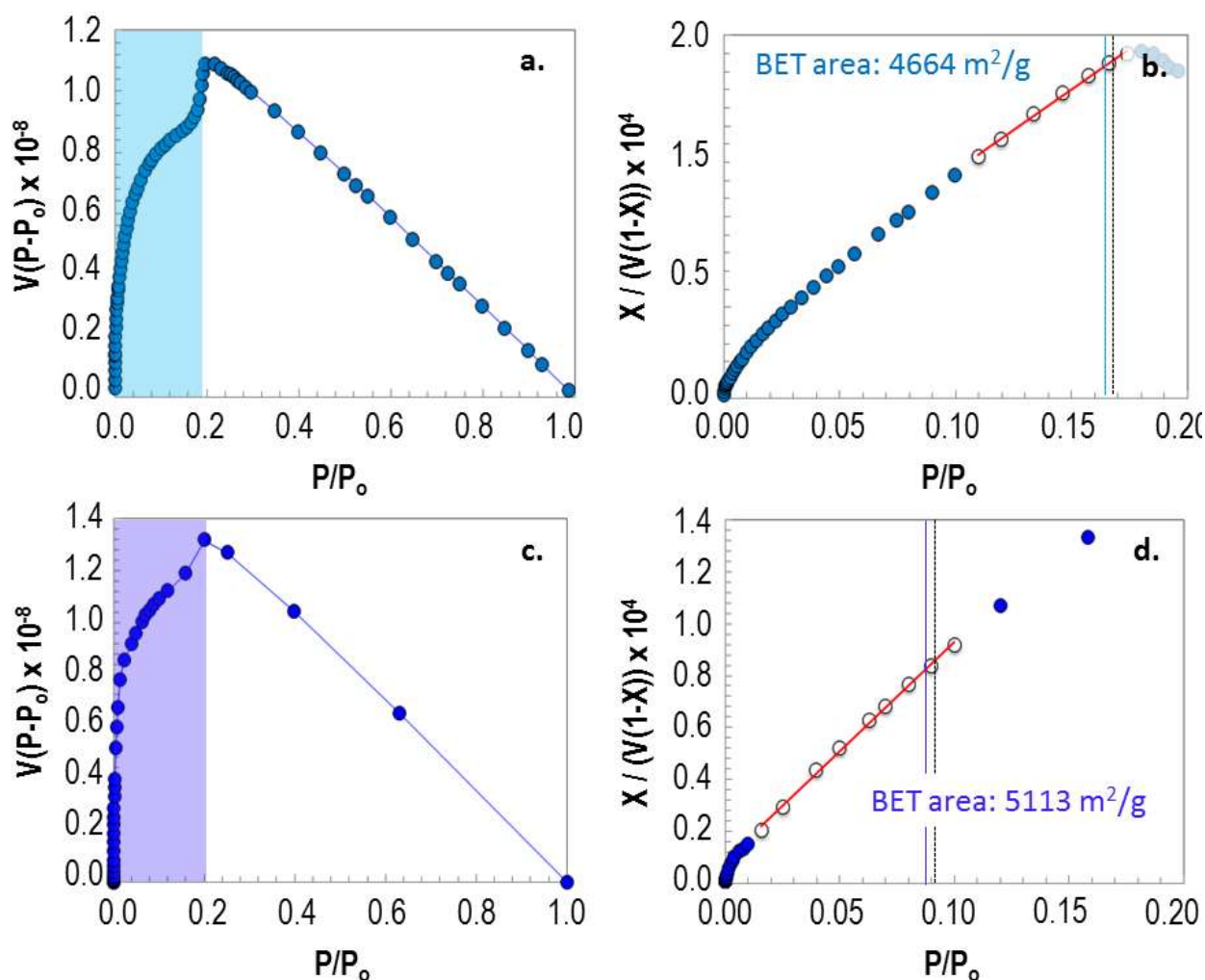


Figure S20. a-b) Plots for the determination of BET area of **she-MOF-2** from the experimental nitrogen isotherm. a) Plot to determine the region in which the first consistency criterion is fulfilled (region in cyan). b) Plot to determine the BET region for the linear regression. Points used in the linear regression are shown in white. Pressure corresponding to the monolayer loading indicated by the vertical cyan line. Pressure value obtained from $1/(\sqrt{C} + 1)$ indicated by the vertical dashed line. c-d) Plots for the determination of BET area of **she-MOF-2** from the simulated nitrogen isotherm. c) Plot to determine the region in which the first consistency criterion is fulfilled (region in blue). d) Plot to determine the BET region for the linear regression. Points used in the linear regression are shown in white. Pressure corresponding to the monolayer loading indicated by the vertical blue line. Pressure value obtained from $1/(\sqrt{C} + 1)$ indicated by the vertical dashed line.

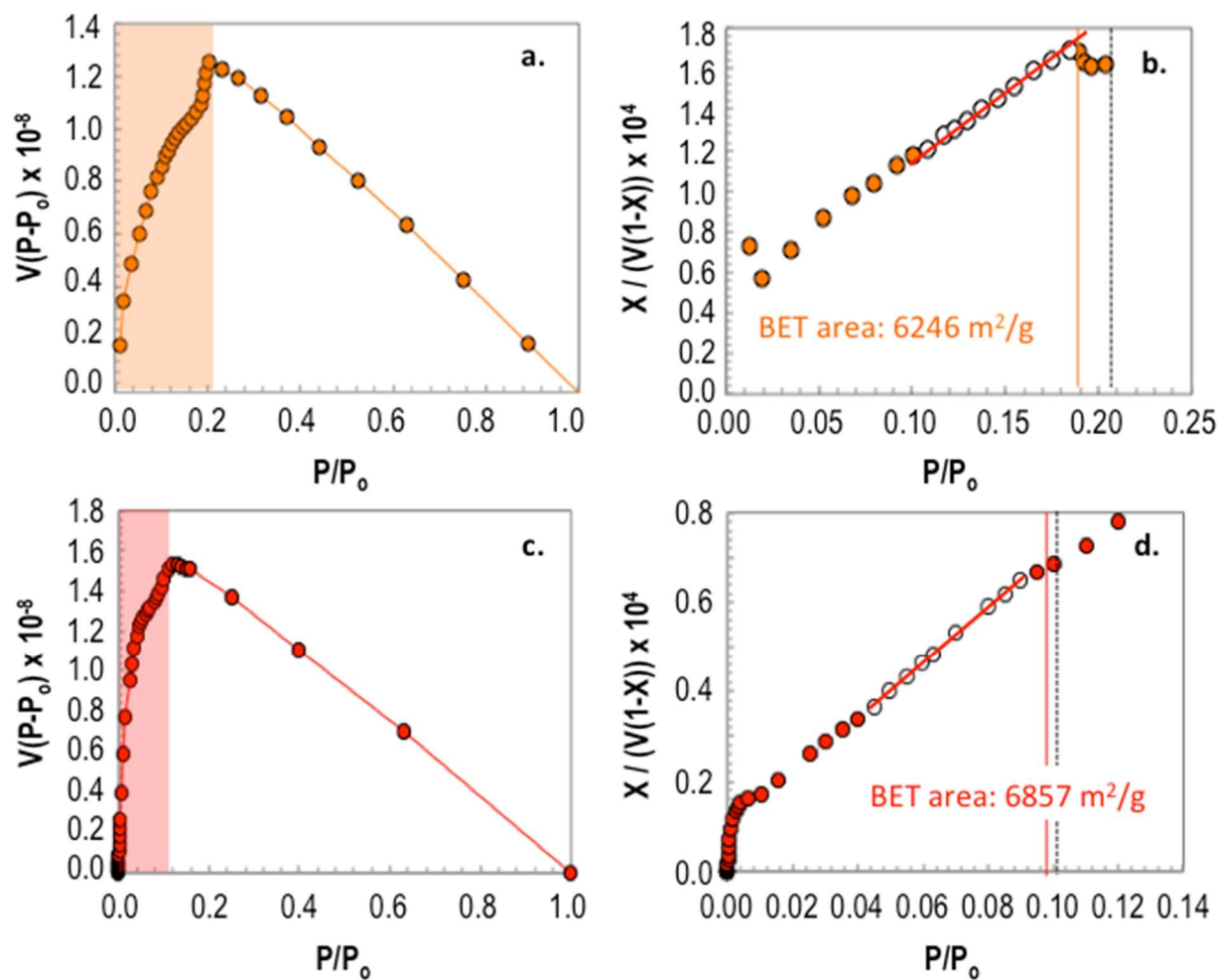


Figure S21. a-b) Plots for the determination of BET area of NU-1103 from the experimental nitrogen isotherm. a) Plot to determine the region in which the first consistency criterion is fulfilled (region in orange). b) Plot to determine the BET region for the linear regression. Points used in the linear regression are shown in white. Pressure corresponding to the monolayer loading indicated by the vertical cyan line. Pressure value obtained from $1/(\sqrt{C} + 1)$ indicated by the vertical dashed line. c-d) Plots for the determination of BET area of NU-1103 from the simulated nitrogen isotherm. c) Plot to determine the region in which the first consistency criterion is fulfilled (region in red). d) Plot to determine the BET region for the linear regression. Points used in the linear regression are shown in white. Pressure corresponding to the monolayer loading indicated by the vertical blue line. Pressure value obtained from $1/(\sqrt{C} + 1)$ indicated by the vertical dashed line.

Section S10. Hydrogen adsorption measurements

High-pressure hydrogen adsorption isotherms were measured at the NIST Center for Neutron Research using a computer controlled Sieverts apparatus, details of which have been published in elsewhere.³⁸ The samples were thoroughly outgassed to remove residual solvents and sample handling was performed in a helium glove box. All gases were of Scientific grade, with a minimum purity of 99.999%. The apparatus measures excess adsorption. Conversion to total adsorption was done by adding the product of gas bulk density at the relevant pressure times the pore volume of the sample to the excess uptake. The gas bulk density was obtained from NIST (<http://webbook.nist.gov/chemistry/fluid/>) and the pore volume was derived from the measured nitrogen saturation loading at 77 K.

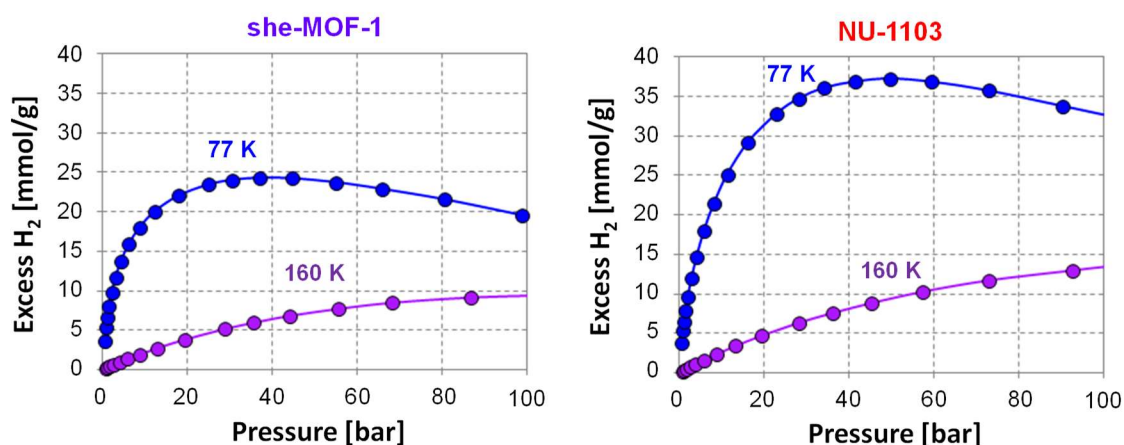


Figure S22. Measured excess gravimetric hydrogen adsorption in **she-MOF-1** and **NU-1103**.

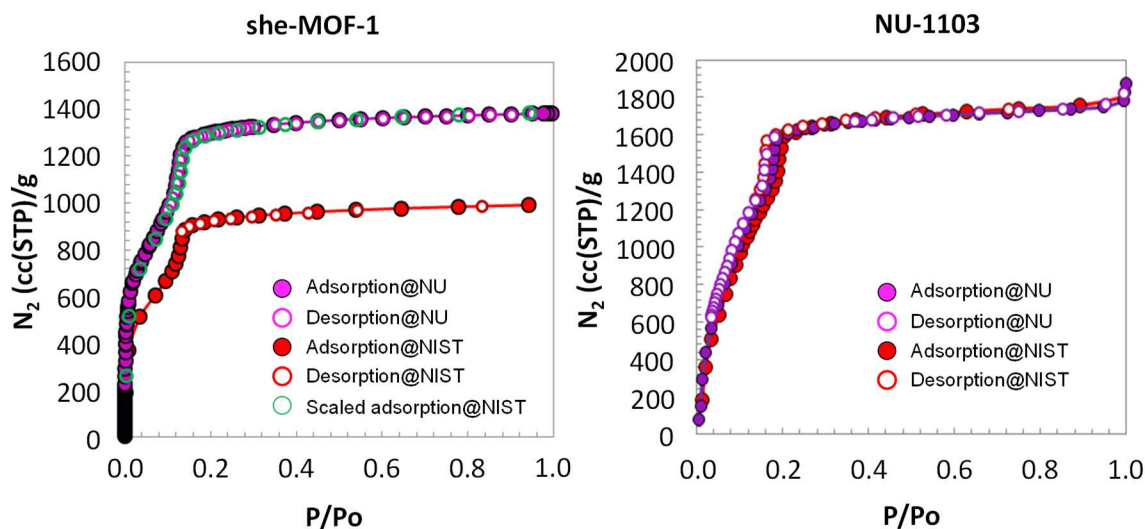


Figure S23. Measured nitrogen isotherms in **she-MOF-1** and **NU-1103**. There was a gap of a few weeks between the measurement at NU and NIST for **she-MOF-1** (pore volume decreased

by ca. 28%). There was a gap of two years between the measurement at NU and NIST for NU-1103 (pore volume remained the same).

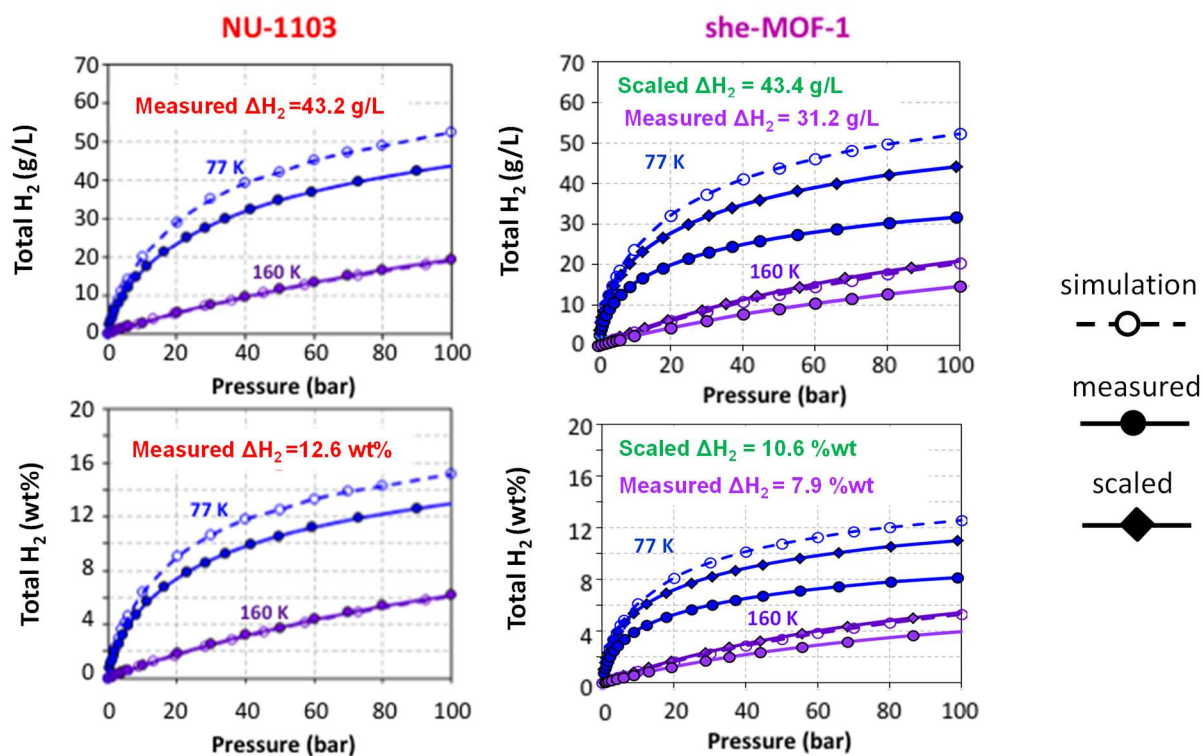


Figure S24. Comparison of volumetric (top row) and gravimetric (bottom row) simulated (dashed line) and measured/scaled (solid line with circle/diamond symbols) hydrogen isotherms for NU-1103 and she-MOF-1. The measured/scaled deliverable capacity (ΔH_2) is annotated in the plots.

Section S11. References

1. Gomez-Gualdron, D. A.; Gutov, O. V.; Krungleviciute, V.; Borah, B.; Mondloch, J. E.; Hupp, J. T.; Yildirim, T.; Farha, O. K.; Snurr, R. Q., Computational Design of Metal–Organic Frameworks Based on Stable Zirconium Building Units for Storage and Delivery of Methane. *Chem. Mater.* **2014**, *26*, (19), 5632-5639.
2. Wang, T. C.; Bury, W.; Gomez-Gualdron, D. A.; Vermeulen, N. A.; Mondloch, J. E.; Deria, P.; Zhang, K.; Moghadam, P. Z.; Sarjeant, A. A.; Snurr, R. Q.; Stoddart, J. F.; Hupp, J. T.; Farha, O. K., Ultrahigh surface area zirconium MOFs and insights into the applicability of the BET theory. *J. Am. Chem. Soc.* **2015**, *137*, (10), 3585-91.
3. *Materials Studio*, Accelrys Software Inc.: San Diego, CA., USA, 2001-2011.
4. Rappe, A. K.; Casewit, C. J.; Colwell, K. S.; Goddard, W. A.; Skiff, W. M., UFF, a full periodic table force field for molecular mechanics and molecular dynamics simulations. *J. Am. Chem. Soc.* **1992**, *114*, (25), 10024-10035.
5. Addicoat, M. A.; Vankova, N.; Akter, I. F.; Heine, T., Extension of the Universal Force Field to Metal–Organic Frameworks. *J. Chem. Theo. Comput.* **2014**, *10*, (2), 880-891.
6. Bureekaew, S.; Amirjalayer, S.; Tafipolsky, M.; Spickermann, C.; Roy, T. K.; Schmid, R., MOF-FF - A flexible first-principles derived force field for metal-organic frameworks. *physica status solidi (b)* **2013**, *250*, (6), 1128-1141.
7. Cavka, J. H.; Jakobsen, S.; Olsbye, U.; Guillou, N.; Lamberti, C.; Bordiga, S.; Lillerud, K. P., A new zirconium inorganic building brick forming metal organic frameworks with exceptional stability. *J. Am. Chem. Soc.* **2008**, *130*, (42), 13850-1.
8. Gutov, O. V.; Bury, W.; Gomez-Gualdron, D. A.; Krungleviciute, V.; Fairen-Jimenez, D.; Mondloch, J. E.; Sarjeant, A. A.; Al-Juaid, S. S.; Snurr, R. Q.; Hupp, J. T.; Yildirim, T.; Farha, O. K., Water-stable zirconium-based metal-organic framework material with high-surface area and gas-storage capacities. *Chem. Eur. J.* **2014**, *20*, (39), 12389-93.
9. Eddaoudi, M.; Kim, J.; Rosi, N.; Vodak, D.; Wachter, J.; O'Keeffe, M.; Yaghi, O. M., Systematic design of pore size and functionality in isoreticular MOFs and their application in methane storage. *Science* **2002**, *295*, (5554), 469-72.
10. Peng, Y.; Srinivas, G.; Wilmer, C. E.; Eryazici, I.; Snurr, R. Q.; Hupp, J. T.; Yildirim, T.; Farha, O. K., Simultaneously high gravimetric and volumetric methane uptake characteristics of the metal-organic framework NU-111. *Chem. Commun.* **2013**, *49*, (29), 2992-4.
11. Chui, S. S., A Chemically Functionalizable Nanoporous Material [Cu₃(TMA)₂(H₂O)₃]_n. *Science* **1999**, *283*, (5405), 1148-1150.
12. Dubbeldam, D.; Calero, S.; Ellis, D. E.; Snurr, R. Q., RASPA: molecular simulation software for adsorption and diffusion in flexible nanoporous materials. *Mol. Sim.* **2016**, *42*, (2), 81-101.
13. Getman, R. B.; Bae, Y. S.; Wilmer, C. E.; Snurr, R. Q., Review and analysis of molecular simulations of methane, hydrogen, and acetylene storage in metal-organic frameworks. *Chem Rev* **2012**, *112*, (2), 703-23.
14. Michels, A.; de Graaff, W.; Ten Seldam, C. A., Virial coefficients of hydrogen and deuterium at temperatures between -175°C and +150°C. Conclusions from the second virial coefficient with regards to the intermolecular potential. *Physica* **1960**, *26*, (6), 393-408.
15. Darkrim, F.; Levesque, D., Monte Carlo simulations of hydrogen adsorption in single-walled carbon nanotubes. *J. Chem. Phys.* **1998**, *109*, (12), 4981.
16. Potoff, J. J.; Siepmann, J. I., Vapor–liquid equilibria of mixtures containing alkanes, carbon dioxide, and nitrogen. *AIChE J.* **2001**, *47*, (7), 1676-1682.
17. Bae, Y.-S.; Yazaydin, A. O.; Snurr, R. Q., Evaluation of the BET Method for Determining Surface Areas of MOFs and Zeolites that Contain Ultra-Micropores. *Langmuir* **2010**, *26*, (8), 5475-5483.
18. Myers, A. L.; Monson, P. A., Adsorption in porous materials at high pressure: Theory and experiment. *Langmuir* **2002**, *18*, (26), 10261-10273.

19. Karavias, F.; Myers, A. L., Isosteric heats of multicomponent adsorption: thermodynamics and computer simulations. *Langmuir* **1991**, 7, (12), 3118-3126.
20. Willems, T. F.; Rycroft, C. H.; Kazi, M.; Meza, J. C.; Haranczyk, M., Algorithms and tools for high-throughput geometry-based analysis of crystalline porous materials. *Microporous Mesoporous Mater.* **2012**, 149, (1), 134-141.
21. Kobayashi, K.; Kobayashi, N., Synthesis and self-association, absorption, and fluorescence properties of differentially functionalized hexakis(p-substituted-phenylethynyl)benzenes. *J Org Chem* **2004**, 69, (7), 2487-97.
22. Pauly, A. C.; Theato, P., Synthesis and characterization of poly(phenylacetylenes) featuring activated ester side groups. *J. Polym. Sci. A: Polym. Chem.* **2011**, 49, (1), 211-224.
23. Ballesteros, L. M.; Martín, S.; Momblona, C.; Marqués-González, S.; López, M. C.; Nichols, R. J.; Low, P. J.; Cea, P., Acetylene Used as a New Linker for Molecular Junctions in Phenylene–Ethynylene Oligomer Langmuir–Blodgett Films. *J. Phys. Chem. C* **2012**, 116, (16), 9142-9150.
24. Lu, Q.; Liu, K.; Zhang, H.; Du, Z.; Wang, X.; Wang, F., From tunneling to hopping: a comprehensive investigation of charge transport mechanism in molecular junctions based on oligo(p-phenylene ethynylene)s. *ACS Nano* **2009**, 3, (12), 3861-8.
25. Zhu, B.; Chen, H.; Lin, W.; Ye, Y.; Wu, J.; Li, S., Template-directed synthesis of flexible porphyrin nanocage and nanorings via one-step olefin metathesis. *J. Am. Chem. Soc.* **2014**, 136, (43), 15126-9.
26. Vadnais, R.; Beaudoin, M. A.; Beaudoin, A.; Heinrich, B.; Soldera, A., Study of the influence of ester orientation on the thermal stability of the smectic C phase: experimental investigation. *Liquid Crystals* **2008**, 35, (3), 357-364.
27. Nelson, A. P.; Farha, O. K.; Mulfort, K. L.; Hupp, J. T., Supercritical processing as a route to high internal surface areas and permanent microporosity in metal-organic framework materials. *J. Am. Chem. Soc.* **2009**, 131, (2), 458-60.
28. Mondloch, J. E.; Karagiari, O.; Farha, O. K.; Hupp, J. T., Activation of metal-organic framework materials. *CrystEngComm* **2013**, 15, (45), 9258.
29. Bruker APEX2, Bruker AXS Inc.: Madison, Wisconsin, USA, 2010.
30. Bruker SAINT, Data Reduction Software. Bruker AXS Inc.: Madison, Wisconsin, USA, 2009.
31. Sheldrick, G. M. *SADABS*, Program for empirical absorption correction: University of Göttingen, Göttingen, Germany, 2008.
32. Farrugia, L. J., WinGX suite for small-molecule single-crystal crystallography. *J. Appl. Crystallogr.* 1999, 32, (Copyright (C) 2012 American Chemical Society (ACS). All Rights Reserved.), 837-838.
33. Sheldrick, G. M., Phase annealing in SHELX-90: direct methods for larger structures. *Acta Crystallogr., Sect. A: Found. Crystallogr.* 1990, A46, (Copyright (C) 2012 American Chemical Society (ACS). All Rights Reserved.), 467-73.
34. Sheldrick, G. M. *SHELXL-97*, Program for structure refinement: University of Göttingen, Göttingen, Germany, 1997.
35. Sheldrick, G. M., A short history of SHELX. *Acta Crystallogr., Sect. A: Found. Crystallogr.* **2008**, A64, (Copyright (C) 2012 American Chemical Society (ACS). All Rights Reserved.), 112-122.
36. Spek, A. L., Single-crystal structure validation with the program PLATON. *J. Appl. Crystallogr.* **2003**, 36, (Copyright (C) 2012 American Chemical Society (ACS). All Rights Reserved.), 7-13.
37. Rouquerol, J.; Rouquerol, F.; Llewellyn, P.; Maurin, G.; Sing, K. S., *Adsorption by Powders and Porous Solids: Principles, Methodology and Applications*. Academic Press: London, 2013.
38. Peng, Y.A. Krungleviciute V., Eryazici, I., Hupp, J.T., Farha, O.K. Yildirim, T., Methane storage in metal-organic frameworks: current records, surprise findings, and challenges. *J. Am. Chem.Soc.* 2013, 135, (32), 11887-11894